Nam *et al. Genome Medicine* (2026) 18:46
https://doi.org/10.1186/s13073-026-01620-2

Genome Medicine

RESEARCH Open Access

In vivo adenine base editing of mutant *Galc* gene ameliorates Krabbe disease progression

Bae-Geun Nam[1,2,3†], Jung Hwa Seo[1,4†], Sung-Ah Hong[2], Ju-Hee Kim[1,5], Minju Kang[1,5], Geneva Rose Notario[1,5], Yoontaik Hong[6], Seunghee Cho[6], Sangsu Bae[2,7,8*] and Sung-Rae Cho[1,3,4,5,9,10,11*]

Abstract

Background Krabbe disease (KD) is caused by mutation of the galactosylceramidase (*GALC*) gene, leading to deficient sphingolipid metabolism, which is essential for functional myelination. The twitcher (*Galc*$^{twi/twi}$) mouse, a KD model with a premature termination codon (PTC) caused by a single-nucleotide G-to-A substitution at the 355th codon of the *Galc* gene, is a model candidate for treatment with adenine base editors (ABEs). ABEs have emerged exclusively among genome editing systems as viable therapeutic candidates to correct mutant genes.

Methods To confirm base editing efficiency of ABEs, mouse embryonic fibroblasts (MEFs) or mutant GALC HEK293T cells treated with three ABE variants (ABEmax, ABE8eWQ, ABE8e) were assessed using targeted deep sequencing. Each split-ABE8e vector was packaged into a dual-vector adeno-associated virus serotype 9 (AAV9) system and delivered to twitcher mice via intracerebroventricular injection on postnatal day 1. Thereafter, motor functions and survival rate were evaluated by rotarod test, clasping test and lifespan analysis. Various methods, including next-generation sequencing (NGS), qRT-PCR, enzyme activity assay, and flow cytometry, were used to measure the base correction rate of the target gene and verified restoration of GALC enzyme activity in the brain of ABE8e-treated mice. Additionally, myelin recovery was evaluated in the brain using histological analysis, magnetic resonance imaging (MRI), diffusion tensor imaging (DTI), and transmission electron microscopy (TEM).

Results The ABE8e-treated MEFs and mutant GALC HEK293T cells showed the most effective editing among the ABE variants tested. Three weeks after dual-AAV9 injection, the PTC was corrected in approximately 0.5% of genomic DNA and 5% of mRNA in twitcher mice. ABE8e treatment restored GALC enzymatic activity to approximately 5% of wild-type (WT) levels, while reducing the accumulation of psychosine—a major neurotoxic metabolite—by approximately 47% relative to WT. Moreover, histological analysis, TEM and, DTI and T2-weighted MRI showed preserved myelination and axonal integrity, along with amelioration of myelin deficits in the corpus callosum of ABE-treated twitcher mice. Five weeks after ABE8e administration, body weight recovered to approximately 64% of WT levels, accompanied by an extension of lifespan. In addition, clasping scores and rotarod performance improved to approximately 23% and 64% of WT levels, respectively.

†Bae-Geun Nam and Jung Hwa Seo contributed equally to this work.

*Correspondence:
Sangsu Bae
sbae7@snu.ac.kr
Sung-Rae Cho
srcho918@yuhs.ac

Full list of author information is available at the end of the article

Conclusions These data demonstrate a reliable application of base editing technology using ABEs as a potential treatment option for KD, progressing the development of therapeutics treating various genetic diseases.

Keywords Krabbe disease, Galc, adenine base editor, adeno-associated virus 9, myelination

Graphical Abstract

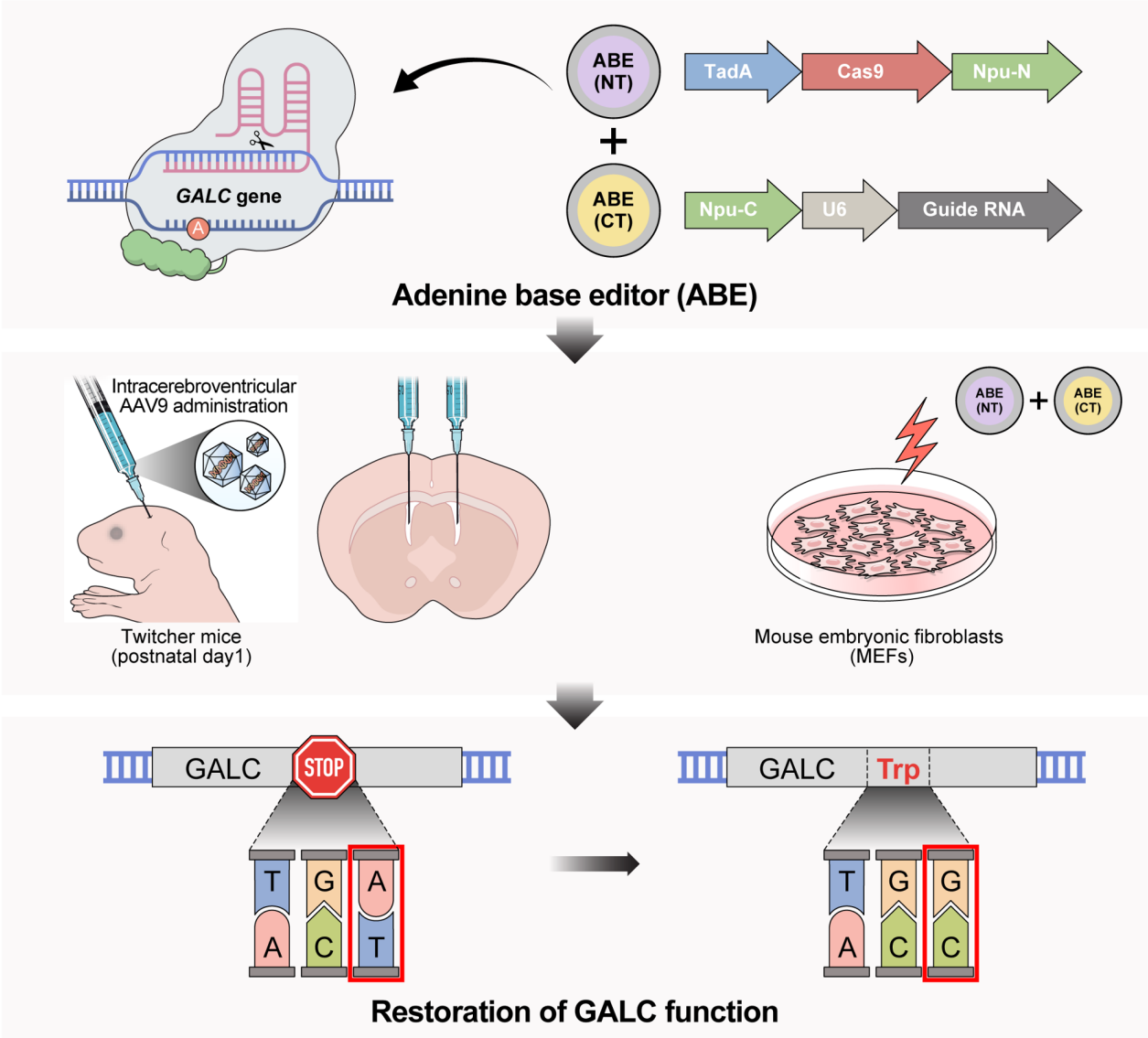

Background

Krabbe disease (KD), also known as globoid cell leukodystrophy, is classified as a lysosomal storage disease. KD occurs in about one in 100,000 to 1 in 250,000 births [1]. Symptoms of infantile KD, the most common form, include muscle weakness, irritability, stiff posture, and developmental delays. Due to the severity of the disease, patients with KD rarely survive beyond 2 years of age [2, 3]. KD is caused by a recessive point mutation of the galactosylceramidase (*GALC*) gene encoding the GALC enzyme essential for catalyzing the decomposition of psychosine, resulting in the malfunction of the nervous system [4, 5]. In KD, the deficiency of GALC enzymes prompts the accumulation of endogenous psychosine, leading to oligodendrocyte death, demyelination, and neuropathological events. To relieve symptoms or treat the disease, several strategies have been employed thus far. One of the most effective methods is *GALC* gene transfer using various adeno-associated virus (AAV) serotypes. Application of this treatment in KD canine

and murine models showed effective results in relieving many symptoms of KD [4, 5]. Another effective treatment currently in use is hematopoietic stem cell transplantation which delays the worsening of disease symptoms and increases the lifespan of KD patients [6, 7]. However, both preclinical and clinical treatments have a limitation in that they do not fundamentally restore the function of the mutant *GALC* gene. Therefore, there is a need to develop approaches that directly target the mutations in the *Galc* gene, the underlying cause of KD, using genome editing tools.

While the CRISPR-Cas9 system is a widely used genome editing tool for treating many genetic disorders, several studies have reported that Cas9-mediated DNA double strand breaks (DSBs) frequently induce chromosomal rearrangements including chromosomal depletion and translocation, p53-driven cell death, or cellular senescence [8–11]. Genome editing via base editors (BEs), primarily cytosine base editors (CBEs) and adenine base editors (ABEs), can circumvent these common defects from CRISPR-Cas9 because they can be used for base conversion without generating DSBs [12, 13]. In particular, ABEs that consist of adenosine deaminase and a partially inactivated Cas9 nickase (nCas9) are capable of A-to-G conversion, which is convenient to bypass a premature termination codon (PTC). The most widely used ABEs are ABEmax containing TadA7.10 and ABE8e containing TadA8e, named according to the evolved version of tRNA-specific adenosine deaminase (TadA) from *Escherichia coli* [14]. Not only did ABE8e exhibit high editing efficiency in the correction of G-to-A mutations of human-derived cells [14, 15], but in vivo ABE8e delivery using dual-AAV systems enabled efficient editing in mouse models of neurological disorders such as Usher syndrome type 1 F and adrenoleukodystrophy [15, 16].

In this study, we used twitcher ($Galc^{twi/twi}$) mice, which serve as a model of spontaneous KD and carry a PTC in the *GALC* gene. This mutation results in the production of a truncated, non-functional GALC enzyme, and the mutant mRNA is subsequently degraded through the nonsense-mediated mRNA decay (NMD) pathway [17]. We previously proposed a more precise version of the ABE with D108Q/V106W mutations, named ABE8eWQ, which reduced both cytosine deamination activity and off-target RNA editing [18]. Altogether, we applied three ABE platforms, ABEmax, ABE8e, and ABE8eWQ, to directly convert the genetic mutation causing PTC on *GALC* gene in this study. We first demonstrated the three ABEs in cells containing *Galc* gene mutation, and further applied ABE8e, which showed the highest editing efficiency, for KD mice via AAV9. For in vivo treatment, ABE platforms were split and packaged in dual-vector AAV9, due to the small viral packaging capacity (4.7 kb). After in vivo treatment with ABE, we examined base correction events at genomic DNA and RNA levels and further focused on identifying and measuring improvements in phenotypes such as body weight, brain weight, and lifespan, as well as behavioral improvements in rotarod and clasping tests. We confirmed that the pathological hallmarks of KD such as reduced GALC enzyme activity and psychosine accumulation were alleviated. Moreover, we observed preserved myelination and axonal integrity using transmission electron microscopy (TEM) and magnetic resonance imaging (MRI) in the brain.

Collectively, this study provides in vivo evidence that genomic correction of *GALC* mutations of KD using ABEs is feasible and can yield measurable phenotypic improvement, even at relatively low editing efficiencies. Thus, the safety of ABE treatment using dual AAV9 vectors was also evaluated in twitcher mice, supporting the potential of base editing–based strategies for the treatment of KD.

Methods

Animals and housing conditions

The mutant strain (B6.CE-$Galc^{twi}$/J, JAX comprehensive protocol #000845) was supplied by Jackson Laboratory (Bar Harbor, ME, USA) and maintained under specific pathogen–free conditions. The $Galc^{twi}$ mutation involves a G to A transition at codon 355 of the *Galc* gene, resulting in a premature stop codon [19]. They were crossed to generate wild-type (WT) mice and homozygous twitcher mice. All heterozygous twitcher mice were housed for the same duration in standard cages ($27 \times 22.5 \times 14$ cm^3) for generating homozygous twitcher mice and given food and water *ad libitum* under alternating 12-hours light/dark cycles, according to animal protection regulations.

Vector design and AAV9 production

ABEmax, ABE8eWQ and ABE8e genes were independently contained with the guide RNA and the CMV promoter in two splicing plasmids. To perform the stereotaxic surgery on twitcher mice, the plasmids pAAV200206-YP030 and pAAV200206-YP031 (VectorBuilder, Chicago, IL, USA) were used to generate AAV9 ABE8e - NT (N-terminal Cas9; 8.93×10^{13} GC/mL), AAV9 ABE8e - CT (C-terminal Cas9; 2.56×10^{13} GC/mL) and AAV9 GFP (4.16×10^{13} GC/mL), which were stored at the deep freezer (-80 °C) until use.

Mouse Embryonic Fibroblasts (MEFs) isolation

A pregnant female mouse at 12.5 ~ 13.5 days was euthanized and the abdomen was cut to excise the uterus. All embryo without the head and visceral tissues were placed on a 10-cm petri dish with 15 ml sterile PBS on ice to prevent reversible reactions. The tissues were disaggregated using sterile razor blades in individual cell culture 75T flask dishes and were digested by Trypsin-EDTA

(0.25%) to dissociate cells. Once the MEFs surpassed 85% confluence, they were diluted at a ratio of 1:4 and plated on to 10-cm culture dishes containing fresh fetal bovine serum (FBS)-containing 10% Dulbecco's Modified Eagle's Medium (DMEM) medium. In order to ensure adequate cell viability for electroporation, MEFs were used before passage 5.

Production of mutant GALC HEK293T cells

Lentivirus containing the mutant *GALC* sequence (48 bp) was transfected into HEK293T cells. Infected cells containing the mutant *GALC* sequence (10,538 bp) were selected by ampicillin. The mutant *GALC* sequence consists of not only the mutated base (adenine) but also twitcher sequences.

Electroporation

One day before electroporation, MEFs from homozygous mice were plated in a 24-well plate at 1×10^5 cells per well. ABEmax, ABE8eWQ and ABE8e plasmids (750 ng) and guide RNAs (250 ng) were electroporated into cells using a Neon Transfection System 10ul Kit (Thermo Fisher Scientific, Waltham, MA, USA; MPK1025). Electroporation parameters (1,350 v, 30ms, 1 pulse for MEFs) were set according to manufacturer protocols. Genomic DNA was isolated 72 h after electroporation.

Transfection in mutant GALC HEK293T cells

One day before transfection, mutant GALC HEK293T cells were seeded in a 24-well plate at 1×10^5 cells per well. ABEmax, ABE8eWQ and ABE8e plasmids (750 ng) and guide RNAs (250 ng) were mixed with Opti-MEM (25 μL), and then with Lipofectamine 2000 (2 μL) (Thermo Fisher Scientific; 11668019)- containing Opti-MEM (25 μL). This method was adapted from the manufacturer's protocol. Genomic DNA was isolated 72 h after electroporation.

Data base analysis from ClinVar database

Information on genetic variants associated with KD was obtained from the ClinVar database [20, 21]. All reported variants were classified based on their molecular consequence and variant type, and were analyzed to determine candidate mutations editable by CRISPR-Cas9 genome editing tools.

Neonatal stereotaxic surgery

Stereotaxic viral delivery into the brain was conducted on postnatal day 1 (P1). Newborn pups were cryoanesthetized for 1 min, and then injected with 1μL of AAV9 ABE8e (ABE8e – NT and CT: 5×10^9 GC, each) or AAV9 GFP (1×10^{10} GC) into both lateral ventricles with a 32-G Hamilton syringe. We performed intracerebroventricular (ICV) injections in not only newborn twitcher mice but also WT mice to evaluate the safety of injected materials. After the treatments, the mice were returned to their home cage with their mother. All ICV injections followed stereotaxic coordinates: AP + 1.5 mm from Lambda, ML + 0.8/-0.8 mm from Lambda, and DV – 1.5 mm from dura mater.

Mouse sacrifice

At 38 days of age, mice were anesthetized by intraperitoneal injection of ketamine (100 mg/kg; Huons, Gyeonggi-do, Korea) and xylazine (10 mg/kg; Bayer Korea, Seoul, Republic of Korea). The mice were then placed in a dark, quiet cage for over 10 min to allow the anesthesia to take effect. Following transcardial perfusion with 1X PBS, the brain and various organs—including the heart, lungs, liver, spleen, kidneys, spinal cord, and sciatic nerve—were harvested. Samples for molecular analyses were stored at – 80 °C, while those for histological analyses were stored in 30% sucrose at 4 °C.

Genomic DNA (gDNA) extraction

According to protocols included in the DNA extraction kits (MicroGem, Napoli, Italy), tail snips of mice were placed into 20 μL of the extraction mixture, prepared DNA-free water: Histosolv: 10X buffer: prepGEM in a ratio of 79:10:10:1. The samples were incubated in three different stages (First: 52℃ for 5 min, Second: 75℃ for 10 min, Third: 95℃ for 3 min).

RNA isolation

Total RNA was extracted from in vivo samples, including the brain and other organs, using TRIzol reagent (Invitrogen Life Technologies, Carlsbad, CA, USA). Isolated RNA samples were air dried at RT for 30 min to allow remaining washing solution to evaporate, and resuspended in DEPC-treated water. Quantification of RNA was Quantification of RNA measured on Agilent 2100 Bioanalyzer (Agilent Technologies, Palo Alto, CA, USA) with the A260/A280.

Targeted DNA and RNA sequencing

The mRNA was extracted from MEFs and various brain regions, including the olfactory bulb, frontal cortex, corpus callosum, striatum, hippocampus, cerebellum, and brain stem from all groups of mice. Then, to generate complementary DNA (cDNA), reverse transcription was conducted by using ReverTra Ace-α-™ (Toyobo Co., Ltd., Osaka, Japan; FSK-101) according to the manufacturer's instructions. To amplify cDNA, PCR was conducted with SUN-PCR blend (Sun Genetics, Daejeon, Republic of Korea). The PCR products were analyzed using an Illumina MiniSeq instrument (Illumina, San Diego, CA, USA). To obtain the percentage of adenosines edited to inosines, the number of adenosines converted

to guanosines was divided by the total number of adenosines in the products.

High-throughput sequencing

Galc gene target sites were amplified from genomic or cDNA using SUN-PCR blend (Sun Genetics). Then, PCR products were purified using Expin PCR SV mini (GeneAll Biotechnology, Seoul, Republic of Korea) and sequenced using a MiniSeq Sequencing System (Illumina). The results were analyzed using BE-Analyzer [22].

Off-target editing frequencies in genomic DNA

To identify potential off-target sequences, the Galc sequence was uploaded to the CRISPR RGEN tool Cas-OFFinder [23], then the search parameters were fixed with the following conditions: mismatch ≤ 3, DNA bulge ≤ 1, and RNA bulge ≤ 1. Off-target sites were amplified from SUN-PCR blend (Sun Genetics) and PCR products were purified using Expin PCR SV mini (GeneAll) and sequenced using a MiniSeq Sequencing System (Illumina). The results were analyzed using BE-Analyzer [22].

Quantitative Real-Time-Polymerase Chain Reaction (qRT-PCR)

qRT-PCR was conducted in triplicate using 2XqPCRBIO SyGreen Mix (PCR Biosystems, London, UK; PB20.12-05), with thermocycler conditions as follows: amplifications start with a template preincubation step at 95 °C for 300 s, followed by 45 cycles at 95 °C for 10 s, 60 °C for 10 s, and 72 °C for 10 s. The oligonucleotide primers are reported in Additional file 1: Table S1 and Table S2.

Prediction three-dimensional protein structure with the bystander A to G converting

Two independent FASTQ files were uploaded in the CRISPResso2 base editor paired end reads mode, and the corresponding amplicon and sgRNA spacer sequences were provided for analysis [24]. Representative protein structures were generated by submitting amino acid sequences to the AlphaFold3 server [25]. Specific interactions among amino acid residues were confirmed using the RCSB PDB online database [26].

Behavioral assessments

KD is usually characterized by a tremendous collapse in myelination and the nervous system, leading to a degeneration of locomotor and neuromuscular behavioral functions [27–30]. Prior to confirming behavioral improvements following in vivo ABE treatments, we examined physical phenotypes and behavioral performances of twitcher mice (i.e., homozygous $Galc^{twi/twi}$) and compared them with WT, heterozygous (i.e., $Galc^{twi/+}$) mice. Previous studies have confirmed that heterozygous carriers did not exhibit neurological damage or impairments in behavioral or motor function, as KD an autosomal recessive disorder [31, 32].

Rotarod test:The rotarod test was used to assess motor coordination and locomotor function. For this assessment, mice were placed on a rotarod treadmill (Ugo Basie, Gemonio (VA), Italy), and their latency to fall, which is the length of time the animals remained on the rolling rod, was measured. Rotarod tests were then performed weekly for five weeks at the constant speed (4 rpm). The latency period was measured in the third trial for each test, and the individual tests were terminated at a maximum latency of 300 s.

Clasping test:The clasping test is used to assess exploratory behaviors and locomotor asymmetry in various neurodegenerative disease mouse models. For this assessment, mice at 3–5 weeks of age were measured in one trial and suspended in the air for 10 s. The scoring standard for this test is clasping time of the hind legs, with 0 points for 0 s, 1 point for 1 to 5 s, 2 points for 5 to 10 s, and 3 points for 10 s.

GALC enzyme activity

GALC enzyme activity was measured via competitive inhibition of β-galactosidase. The corpus callosum of the brain was homogenized in distilled water on ice with a pellet pestle. Lysates were then sonicated two times for 20 s on ice. A mixture containing total 20 μg of brain homogenate and GALC substrate (6HMU-β-d-galactoside; Moscerdam Substrates, Rotterdam, Netherlands) was incubated for 17 h at 37 °C. Enzymatic activity was measured on a spectrofluorometer (λex 404 nm; λem 460 nm) via fluorescence measured with an Envision HTS multimode plate reader (PerkinElmer, Hamburg, Germany).

Psychosine quantification

Fresh frozen mouse brain hemispheres were homogenized in PBS in microcentrifuge ultra low-adhesion tubes (Tarsons Products, West Bengal, India). Protein quantification was performed using the Bradford assay. 4.2 μl of N, N-dimethyl psychosine (Avanti Polar Lipids, Alabaster, USA), used as internal standard (ISTD), 2 ml of MeOH, and 1 mL of chloroform were added to each sample. Samples were sonicated for 60s and incubated for overnight at 48 °C. The following day, samples were gradually brought up to room temperature and 452 μL of KOH (1 M) was added. Samples were sonicated for 60s and incubated for 3 h at 37 °C. 24.4 μL of glacial acetic acid was added to each tube, and then each was vortexed for 20s. 200uL of each sample was dried overnight at 25 °C a centrifugal evaporator (CVE-3000; EYELA, Tokyo, Japan). The following day, 400μL of chloroform: methanol (1:2, v/v) was added to each sample before centrifugation, and supernatant was collected. Psychosine

concentrations were quantified using high-resolution LC-MS (Orbitrap Exploris 240; Thermo Fisher).

Immunohistochemistry (IHC)

Mouse brain samples were frozen quickly in isopentane with dry ice, and sectioned into 16 μm thick slices by cryostat (Leica Microsystems, Austria). Brains were sectioned coronally and sections including the corpus collosum were selected for immunohistochemical analysis of myelin basic protein (MBP). Anti-MBP (1:1000; Abcam, Cambridge, UK) primary antibody and Alexa Fluor 594 goat anti-mouse (1:400; Invitrogen) secondary antibody were used for immunostaining. Immunostained slides were mounted with Vectashield mounting medium with 4′, 6 - diamidino-2-phenylindole (DAPI; Vector, Burlingame, CA, USA) and analyzed using M2 microscopy (Zeiss, Gottingen, Germany).

Diffusion Tensor Imaging (DTI) metric acquisition and comparison

Mice were anesthetized with 1–2% isoflurane at postnatal day 38. The images were acquired using a 9.4 T Biospec scanner (Bruker, Ettlingen, Germany) running Paravision 5.1, using a 40 mm transceiver coil. Anatomical images were obtained according to the rapid acquisition with relaxation enhancement (RARE) protocol. Diffusion experiments were conducted using the diffusion tensor imaging (DTI) echo planar imaging (DTI-EPI) protocol and processed in DSI studio software. DTI data were analyzed in MATLAB (MathWorks, Natick, MA). Comparisons were then made between each group by four kinds of DTI parameters: fractional anisotropy (FA), axial diffusivity (AD), radial diffusivity (RD) and mean diffusivity (MD). The imaging parameters: slice thickness, 0.32 mm; number of slices, 20; matrix size, 128 × 128; matrix resolution, 0.156 × 0.156 mm; 4/10 ms; 30 directions with b = 670 s/mm2; and TE/TR = 23.5/5000 ms.

Luxol Fast Blue (LFB)/Periodic Acid Schiff (PAS) staining

Mouse brain samples were fixed in 4% paraformaldehyde at 4 °C and embedded in paraffin wax. Coronal Sect. (4 μm thick) including the corpus callosum were prepared from paraffin-embedded tissues. Deparaffinized sections were incubated overnight at 70 °C in 0.1% Luxol Fast Blue solution (Solvent Blue 38; Sigma-Aldrich, MO, USA), which stains myelin blue. Sections were washed in tap water, and differentiated by dipping in 0.05% lithium carbonate solution and 70% ethanol until the gray matter became transparent. Subsequently, PAS staining was performed by oxidation with 0.05% periodic acid in 1 N HCl, followed by Schiff reagent (Sigma-Aldrich) incubation for 15 min, sulfurous rinses, and hematoxylin counterstaining. After dehydration, all sections were cleared by xylene and mounted with mounting solution. Images were captured using a bright-field microscope (Olympus BX43; Olympus, Center Valley, PA), and the total number of PAS^+ cells, defined as cells showing dark pink cytoplasmic staining, were counted in the corpus callosum.

Transmission Electron Microscopy (TEM)

Electron microscopic analysis of the corpus callosum was performed. Mouse brains were prepped at postnatal day 38 and immediately fixed in 0.1 M phosphate buffer followed by 4% PFA containing 2% glutaraldehyde (MERCK, Darmstadt, Germany) for more than 12 h. The samples were postfixed with 1% osmium tetroxide dissolved in 0.1 M phosphate buffer for 2 h, dehydrated in ethanol and infiltrated with propylene oxide. Embedding solution was a Poly/Bed 812 kit (Polysciences, Warrington, PA, U.S.A). For counter staining, 70 nm thick ultra-thin slices were stained with 6% uranyl acetate (EMS, PA, USA; 22,400 for 20 min) and lead citrate (Fisher Scientific; for 10 min). Brain samples were sectioned using a LEICA EM UC-7 (Leica Microsystems) and transferred onto copper and nickel grids. All sections were observed by a transmission electron microscope (JEM-1011; JEOL, Japan).

G-ratio analysis

The g-ratio, defined as the ratio of the inner axonal diameter (D_{axon}) to the total fiber diameter (D_{fiber}) including myelin, was calculated to assess the relative thickness of the myelin sheath.

The g-ratio was calculated for each axon as: $\text{g-ratio} = D_{\text{axon}}/D_{\text{fiber}}$

Lower g-ratios indicate thicker myelin sheaths, whereas higher g-ratios reflect thinner myelination For quantitative analysis, randomly selected myelinated axons in each mouse were measured, and mean g-ratios were compared among groups in the corpus callosum using MyelTracer [33].

Hematoxylin and Eosin (H&E) staining

Hematoxylin and eosin (H&E) staining is a well-established technique to examine pathological changes. We differentiated between the nuclear (purple) and cytoplasmic parts (pink) of in vivo tissue. The patterns of coloration showed the distribution of cells and provided a general overview of a histopathological structure. This experiment was conducted to determine whether there were any histological abnormalities like dysplasia.

Statistical analysis

Data are presented as mean ± standard error of the mean (SEM). Statistical differences were assessed using the one-way analysis of variance (ANOVA) test followed by a *post hoc* Bonferroni or chi-square test, as appropriate. Two-way repeated-measures ANOVA was conducted to evaluate the interaction effects between time and group

in the rotarod test, clasping test and measurement of mouse body weight measurements. Kaplan-Meier survival analysis was performed to assess the survival rate. Values indicative of statistical difference are given as follows: $^{*}P < 0.05$, $^{**}P < 0.01$, $^{***}P < 0.001$ in Bonferroni. We used Statistical Package for Social Sciences (SPSS) version 28.0 (IBM Corporation, Armonk, NY, USA) for statistical analysis. All graphs were plotted using GraphPad Prism Version 10 (GraphPad Software, San Diego, CA, USA).

Results

In silico screening of Krabbe disease database to select potential therapeutic candidates

KD is an autosomal recessive disorder caused by mutations in the GALC gene located at the 14q31.3 loci on human chromosome 14. To enable in-depth experimental approaches, it is essential to obtain a comprehensive understanding of the genetic landscape of KD. Therefore, we retrieved genetic variation data from the ClinVar database to determine how many pathogenic variants are potentially targetable by the CRISPR-Cas9 system.

We first analyzed the molecular consequence to classify the major types of disease-causing mutations, including splice-site (6.0%), nonsense (7.9%), frameshift (11.4%), UTR (13.4%), ncRNA (19.1%), and missense variants (42.2%) (Additional file 1: Fig. S1A). We then assessed the distribution of nucleotide variation types, such as indel (1.0%), duplication (4.0%), insertion (5.7%), deletion (9.3%), and single-nucleotide variants (80.1%) (Additional file 1: Fig. S1B). Because approximately 80% of the mutations are single-nucleotide variants, precision genome-editing technologies such as BE and prime editing (PE) are likely to be essential for KD.

Among the 1,169 single-nucleotide mutations identified, 342 mutations (30.4%) were targetable by ABE, 369 (32.8%) by CBE, and 415 (36.9%) by PE, when considering 'NG' protospacer-adjacent motif (PAM) sequences (Additional file 1: Fig. S1C). Of the 342 ABE-editable mutations, we found that 36.0% ($n = 123$) contained NGG PAMs, whereas 64.0% ($n = 219$) contained NGH PAMs (H = A, C, or T) (Additional file 1: Fig. S1D). Therefore, although ABEs have limitations in that they cannot be used to correct most of variants associated with KD, it may be a promising therapeutic approach for the approximately 30% of single-nucleotide variants that are ABE-editable.

A split-ABE platform enables A-to-G conversion in embryonic fibroblasts of twitcher mice

To correct the point mutation, we prepared NG-ABEmax, NG-ABE8e, and NG-ABE8eWQ, based on NG PAM-targetable SpCas9 (Fig. 1A) [34]. All ABE variants were designed dual plasmids in a split form with an intein-mediated reconstitution system, one vector encoding the N-terminus of the ABE and the other encoding the C-terminus of the ABE, with an sgRNA-expression cassette (Fig. 1A). Prior to the in vivo administration of ABE platforms, we examined whether each ABE contained in the dual-AAV9 vector system could convert the point mutation in cells from twitcher mice. For this experiment, we removed and dissociated several embryos from a pregnant heterozygous female at 12.5 ~ 13.5 days to obtain diseased MEFs [35, 36]. After the MEFs underwent sufficient proliferation, the dual-AAV9 vectors were transfected into the cells and genomic DNA (gDNA) from bulk populations were subjected to targeted deep sequencing. Target base A_6 was most efficiently edited by ABE8e (10.77% ± 0.81%), compared to ABEmax (0.79% ± 0.26%) and ABE8eWQ (3.84% ± 0.78%) and a negative control (NC) (0.25% ± 0.02%). On the other hand, ABE8e also showed higher editing frequencies at bystander bases (A_8: 9.83% ± 0.14% and A_{11}: 5.95% ± 1.75%), compared to ABEmax (A_8: 1.24% ± 0.53% and A_{11}: 0.14% ± 0.02%) and ABE8eWQ (A_8: 0.60% ± 0.21% and A_{11}: 0.16% ± 0.03%) and NC (A_8: 0.13% ± 0.02% and A_{11}: 0.18% ± 0.02%) (Fig. 1C). Collectively, we verified base editing activities of various ABEs in MEFs from KD mice and decided to further utilize ABE8e with higher editing efficiency for in vivo therapeutic treatments, given that ABEmax and ABE8eWQ showed less effective editing activities in cells from the twitcher mice.

A split-vector ABE can induce base editing in mutant GALC HEK293T cells

Preliminary in vitro transfection and transduction of the mutant *Galc* gene into HEK293T cells was conducted to confirm the base editing efficiency among split ABEmax, ABE8eWQ and ABE8e genes. After extracting gDNAs from all transfected mutant GALC HEK293T cells, we conducted high-throughput sequencing. The (A_6) target base editing efficiency of transfection was observed in ABEmax (39.95% ± 1.48%), ABE8eWQ (36.05% ± 1.34%) and ABE8e (50.65% ± 3.75%). The (A_8) bystander base editing efficiency of ABE8eWQ (11.20% ± 1.13%) decreased compare to ABEmax (27.75% ± 1.77%) and ABE8e (50.5% ± 3.54%). Additionally, the (A_{11}) bystander base editing efficiency of ABE8e (37.35% ± 3.32%) was higher than split ABEmax (1.00% ± 0.00%) and ABE8eWQ (0.20% ± 0.28%) (Fig. 1D). Consequently, in mutant GALC HEK293T cell experiments, even if the individual ABE gene was split into two plasmids, the base editing efficiency was maintained, as illustrated by the activity of Npu protein compared to control groups [37, 38].

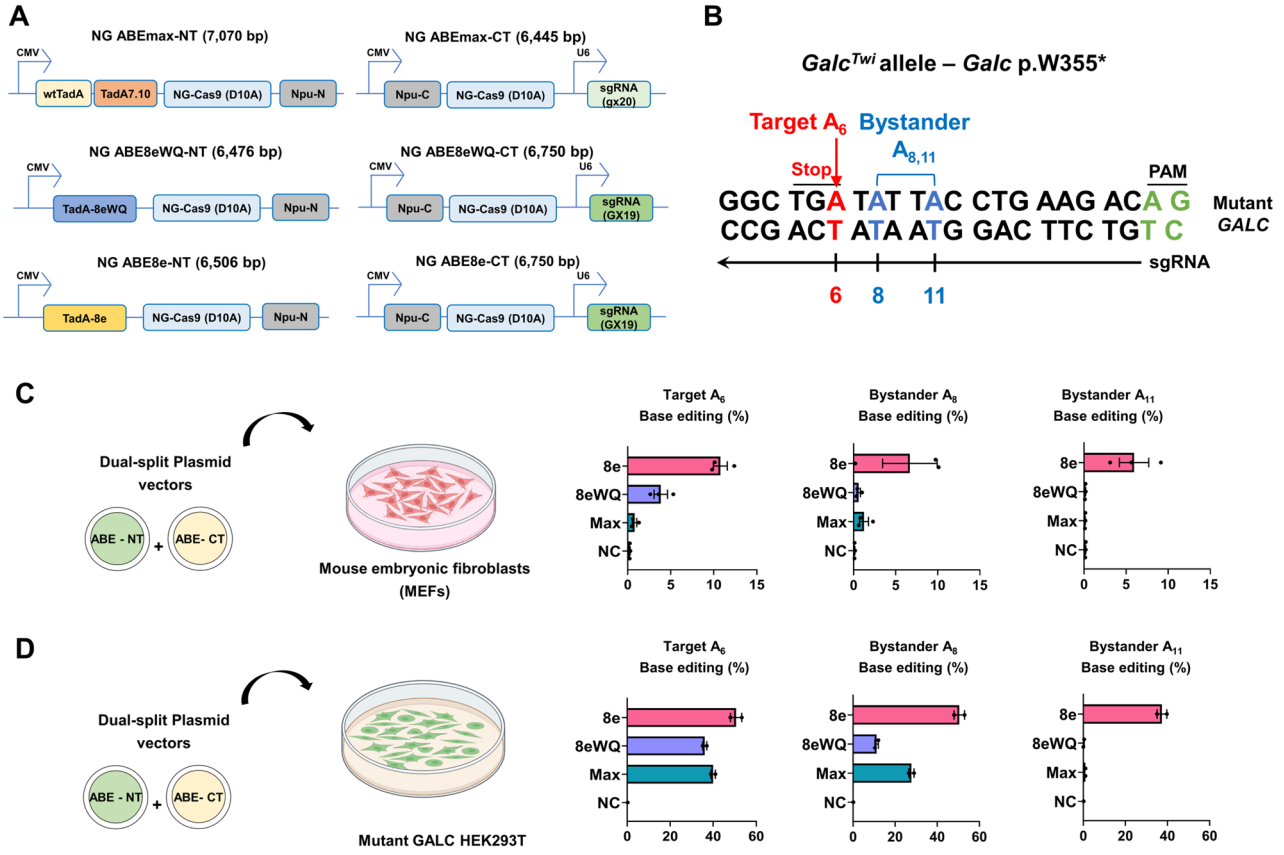

Fig. 1 Gene editing efficiency of three split-ABEs edited mutant *Galc* genes in mouse embryonic fibroblasts. **A** Composition of the individual ABEmax, ABE8eWQ and ABE8e plasmids which are divided into ABE-NT and ABE-CT forms including Npu proteins. **B** The nonsense mutation of twitcher mice in context. The arrow indicates the sgRNA for NG-ABEs and colors indicate the target adenosine (red), bystander adenosine (blue), and PAM site (green). Nucleotide number indicates position, counting the PAM site as positions 21 and 22. **C**, **D** The percentages of (A6) target base editing and (A8 and A11) bystander base editing show the highest efficiency in both MEFs ($n = 3$, each group; Mean ± SEM) and mutant GALC HEK293T cells treated with ABE8e plasmids compared to other groups (NC, $n = 1$; 8e, 8eWQ and Max, $n = 2$; Mean ± SEM)

In vivo administration of ABEs induces base correction of target mutation in the *Galc* gene

Dual-AAV9 vectors for in vivo delivery of the split ABE8e platform were constructed, and 2 µL of the dual-AAV9 (a total of 2×10^{10} GC/µL, containing 1×10^{10} GC of each vector) was bilaterally administered into the lateral ventricles of twitcher mice on P1 [39–41]. AAV9 vectors containing a GFP expression cassette were also prepared as a control. Following treatment, all mice in untreated, GFP- and ABE8e-treated groups were sacrificed on postnatal day 38, and seven brain regions (the olfactory bulb, frontal cortex, corpus callosum, striatum, hippocampus, cerebellum and brain stem) and seven organs (the heart, lung, liver, spleen, kidney, spinal cord and sciatic nerve) were obtained for further analysis.

First, we investigated whether AAV9 vectors were effectively transduced and distributed in the organs and brain of mice. To this end, we measured RNA expression of vectors, i.e., the N-terminus and C-terminus portions of the ABE, in treated mice through qRT-PCR. We consequently observed ABE expression in the brain, mainly in the corpus callosum as well as ABE expression in other organs, mainly the heart, after AAV9 injection (Fig. 2B).

Next, we individually extracted gDNA from the brain tissues of transduced mice and quantified base editing efficiencies using targeted deep sequencing. The ABE8e-treated group showed a trend toward higher base editing efficiency at the target adenine (A_6) in the frontal cortex and corpus callosum (0.26% ± 0.03% and 0.29% ± 0.05%, respectively) compared to the untreated (0.06% ± 0.02% in frontal cortex; 0.09% ± 0.05% in corpus callosum) and GFP-treated groups (0.05% ± 0.04% in frontal cortex; 0.04% ± 0.04% in corpus callosum) (Fig. 2C). Similarly, at the RNA level, most ABE8e-treated twitcher mice showed higher editing efficiencies at the same target base (A_6), particularly in the corpus callosum. The mean base editing efficiency in the ABE8e-treated group was 2.91% ± 0.87%, showing statistical significance (Fig. 2D). Previous studies have reported that cDNA often exhibits higher apparent editing efficiencies than gDNA, likely due to the greater abundance of RNA transcripts relative to genomic DNA [21]. However, across all groups,

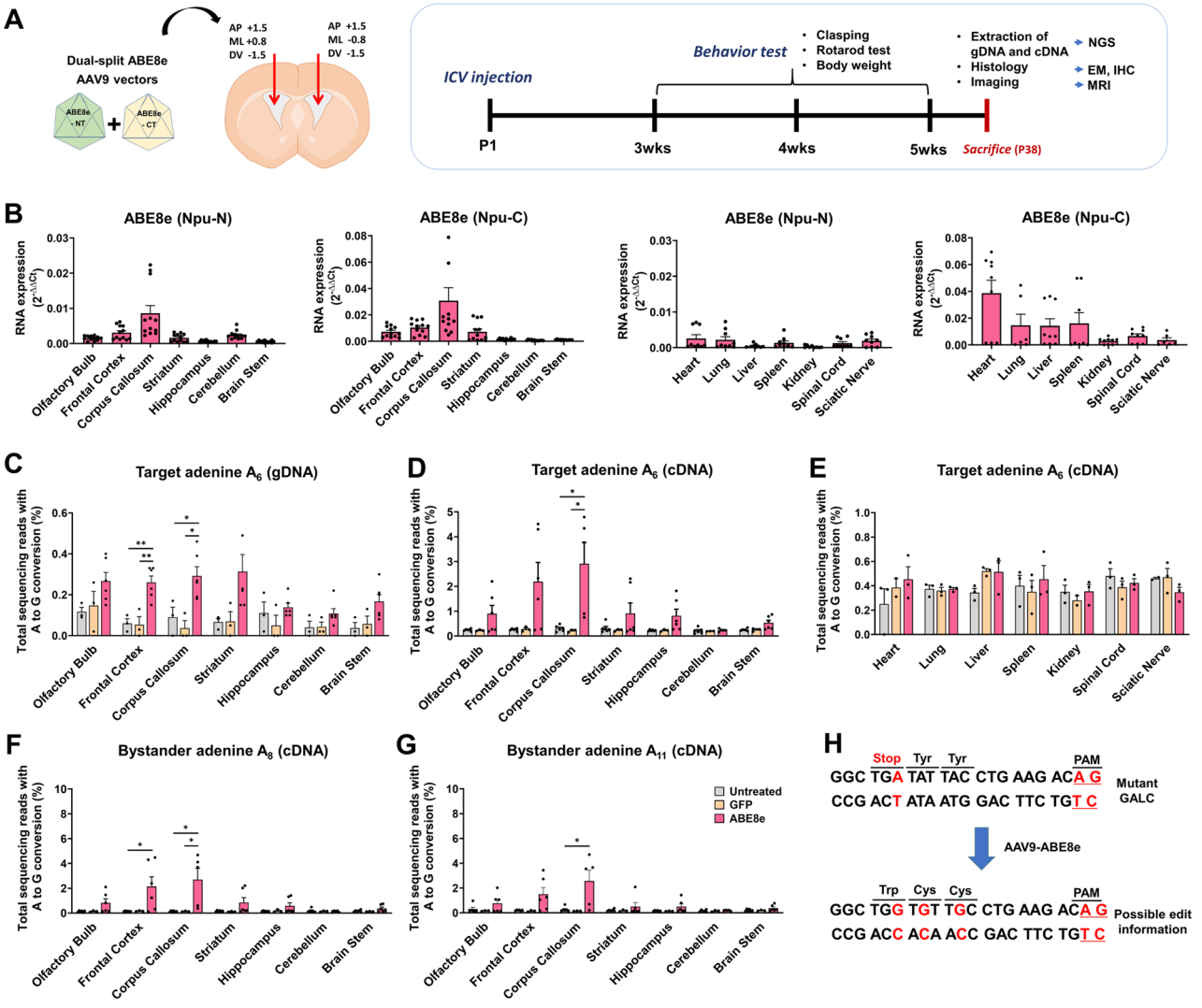

Fig. 2 mRNA expression level of NPU-N and NPU-C and bystander effect of split-ABE8e in ABE-treated mice. **A** Experimental schedule of ICV injection at postnatal day 1 and preparation of seven brain regions and seven tissue regions for gDNA and cDNA extraction to conduct NGS. **B** The mRNA expression levels of NPU-N and NPU-C are representative of the in vivo transduction efficiency of split-ABEs. $2^{-\Delta\Delta Ct}$ value of NPU-N and NPU-C in seven brain regions of ABE8e-treated mice ($n = 12$ from 4 samples, each group). NPU-N and NPU-C in seven tissue regions of ABE8e-treated mice ($n = 9$ from 3 samples, each group). **C** and **D** In both mutant *Galc* gDNA and *Galc* cDNA isolated from transduced brain regions, the percentage of (A6) target base edits was highest overall in ABE8e-treated mice (Untreated, $n = 3$; GFP, $n = 3$; ABE8e, $n = 6$). **E** Percentage of (A6) target base editing in mutant *Galc* cDNA isolated from tissue regions shows a negligible difference between groups ($n = 3$, each group). **F** and **G** Percentage of (A_8 and A_{11}) bystander base edits was high in mutant *Galc* cDNA isolated from transduced brain regions, particularly in the corpus callosum, in ABE8e-treated mice (Untreated, $n = 6$; GFP, $n = 3$; ABE8e, $n = 6$). (H) The dual AAV9-ABE8e induced conversion of two near tyrosines to cysteines in the mutant *Galc* gene. All values are shown as Mean ± SEM with $^{*}P < 0.05$, $^{**}P < 0.01$

RNA-level base editing efficiencies did not show significant variation among the seven examined tissues—heart, lung, liver, spleen, kidney, spinal cord, and sciatic nerve (Fig. 2E).

Concurrently, base editing events in bystander adenines (A_8 and A_{11}) were observed in the ABE8e-treated group in the frontal cortex and corpus callosum, similar to the above observations in MEFs. Bystander edits of A_8 and A_{11} in the ABE8e-treated group were 2.14% ± 0.78% and 1.50% ± 0.54% in the frontal cortex, and 2.69% ± 0.91% and 2.56% ± 0.89% in the corpus callosum, indicating that ABE8e showed overall higher editing activity (Fig. 2F, G). We additionally found that dual-AAV9-ABE8e induced conversion of two near tyrosines to cysteines in the mutant *Galc* gene (Fig. 2H).

To confirm the specific base editing pattern in the ABE8e group, one of the ABE8e-treated mouse samples was analyzed and confirmed using CRISPResseo2 software [24]. In the frontal cortex and the corpus callosum, editing events were observed in the following order: conversion of three adenines within the ABE8e activity window, conversion of two adenines, and conversion

of a single on-target adenine (Additional file 1: Fig. S2A, B). Although indel events by nick Cas9 is markedly lower than those by WT Cas9, they are not completely absent; therefore, their occurrence needed to be examined as well [42, 43]. The indel events were not detected in the frontal cortex and the corpus callosum (Additional file 1: Fig. S2C, D).

Finally, we used the AlphaFold3 software to confirm predicted structures of WT and undesired GALC enzyme which was caused by the bystander A to G conversion. Compared to the wild type GALC enzyme, the undesired GALC enzyme had amino acid substitutions at positions 356 and 357 from tyrosine to cysteine, with no apparent conformational and chemical interaction alterations between those enzyme structures (Additional file 1: Fig.S2 E, F).

Off-target analysis of genomic and mRNA level in mouse samples

Compared to other viral vectors which have been considered for clinical trials, AAVs have longer periods of expression, which can lead to side effects caused by prolonged Cas9 and nCas9 protein level in target cells [44, 45]. Especially, according to a previous study describing ABE-mediated off-target DNA or RNA editing effects [46], sgRNA-independent genomic and mRNA off-targets can occur, when AAV is combined with CRISPR system.

To evaluate the presence of genomic off-target effects, we utilized Cas-OFFinder software [23] with defined criteria which allowed for up to 3 mismatches and 1 DNA/RNA bulge and finally selected 12 potential off-target gene candidates (Fig. 3A). In the frontal cortex and the corpus callosum, where high on-target editing efficiencies were confirmed among various brain regions, the analysis was confined to adenines located within the activity window of ABE8e at each off-target site. Editing efficiencies at all predicted off-target sites remained below 0.3% in untreated, GFP, and ABE8e groups (Fig. 3B, C).

In addition, we also quantified A to I conversions in a few well-known RNA transcripts in ABE8e-treated twitcher mice. In the frontal cortex and the corpus callosum, the number of A to I events in AARS1, PERP, TOPORS and MCM3AP RNA transcripts were not meaningfully different among untreated, GFP- and ABE8e- treated groups (Additional file 1: Fig. S3A, B), indicating that neither ABE8e induced serious RNA off-target editing. This was also confirmed in other tissues, where A to I alterations in RNA transcripts were not significantly different among untreated, GFP- and ABE8e-treated groups in the heart and liver (Additional file 1: Fig. S3C, D).

Verifying features of homozygous twitcher mice as a model of Krabbe disease

Analyses showed that the heterozygous group (7.72 ± 0.24 g at week 3; 12.31 ± 0.44 g at week 4; 16.82 ± 0.44 g at week 5) maintained body weights comparable to those of the WT group (8.242 ± 0.28 g at week 3; 13.471 ± 0.39 g at week 4; 17.43 ± 0.41 g at week 5) during 3 ~ 5 weeks, whereas twitcher mice (6.22 ± 0.11 g at week 3; 7.64 ± 0.15 g at week 4; 7.09 ± 0.13 g at week 5) failed to gain weight during 3 ~ 5 weeks (Fig. 4A) as indicated by significant interactions between time and group (two-way ANOVA, $F = 154.998$, $P < 0.001$) (Fig. 4A and Additional file 1: Fig. S4A). As brain atrophy is one of the representative symptoms of KD [47], brain weight was recorded after sacrifice at postnatal day 38. The heterozygous group (0.47 ± 0.01 g) showed similar brain weights to the WT group (0.47 ± 0.00 g), whereas the twitcher group (0.40 ± 0.01 g) showed significantly reduced values at terminal 38 days of age ($P < 0.001$; Fig. 4B).

Additionally, we conducted several behavioral tests to compare behavioral abilities among the three groups. The clasping scores of the twitcher group showed significant interactions between time and group at 3 ~ 5 weeks of age compared to WT and heterozygous groups (two-way ANOVA, $F = 42.790$, $P < 0.001$), and clasping scores of the twitcher group (1.04 ± 0.09 at week 3; 2.19 ± 0.12 at week 4; 2.85 ± 0.07 at week 5) were clearly higher than the values of WT (0.17 ± 0.09 at week 3; 0.06 ± 0.06 at week 4; 0.00 ± 0.00 at week 5) and heterozygous (0.18 ± 0.07 at week 3; 0.04 ± 0.04 at week 4; 0.00 ± 0.00 at week 5) groups at 3 ~ 5 weeks of age ($P < 0.001$; Fig. 4C and Additional file 1: Fig. S4B).

Moreover, results from the rotarod test showed significant impairment of motor functions in the twitcher group compared WT and heterozygous groups, with significant interactions between time and group at 3 ~ 5 weeks of age (two-way ANOVA, $F = 9.914$, $P < 0.001$). Rotarod performance scores in twitcher mice (231.27 ± 11.73 s at week 3; 234.46 ± 12.40 s at week 4; 114.73 ± 19.68 s at week 5) were significantly lower than those in WT (295.83 ± 3.31 s at week 3; 300.00 ± 0.00 s at week 4; 300.00 ± 0.00 s at week 5) and heterozygous (299.18 ± 0.82 s at week 3; 299.41 ± 0.59 s at week 4; 300.00 ± 0.00 s at week 5) mice during weeks 3 ~ 5 ($P < 0.001$; Fig. 4D and Additional file 1: Fig. S4C). Taken together, we confirmed autosomal recessive twitcher mice as a relevant model of KD and verified that only homozygous recessive mice exhibited key KD pathologies such as loss of body weight and motor abilities.

In vivo base editing with ABEs alleviates behavioral deterioration in twitcher mice

Data analysis using the Pearson's chi-square test revealed that there were no significant differences in

A

OT#	Target sequence	Mismatch #	Bulge #	Gene (Chr:position)
On-target	**GGCTGATATTACCTGAAGAC**AG	0	0	*Galc exon* (chr12)
OT1	GACTGAGTTACCTGAAGACTGG	2	1	Intron *Zfp282* (chr6)
OT2	GGCTGATATTCACCTGGAGTCTGG	2	1	Intergenic lncRNA (chr8)
OT3	GGCTGAAAATAGCCTGAAGACTGG	2	1	Intron *Maml2* (chr9)
OT4	GAATGATTTACCTGAAGACAGG	2	1	*Tcp11x2* exon (chrX)
OT5	GGTCTGTAATAACCTGAAGACTGG	3	1	Intron *Wdr34* (chr2)
OT6	GGCTGAATGGAACCTGAAGACGGG	3	1	Intron *Tshz2* (chr2)
OT7	AGAAGATGATTACCTGAAGACAGG	3	1	Intergenic region (chr5)
OT8	GGCTGAAACCACCTGAAGACAGG	3	0	Intron *Ttc29* (chr8)
OT9	GCAAACATTACCTGAAGACAGG	3	1	Intron *Arhgap20* (chr9)
OT10	GTCTGCTTCACCTGAAGACTGG	3	1	Intergenic region (chr14)
OT11	GGTTGGTATGACCTGAAGACAGG	3	0	Intergenic region (chr15)
OT12	GGAGGAAGTACCTGAAGACTGG	3	1	Intergenic region (chr16)

B

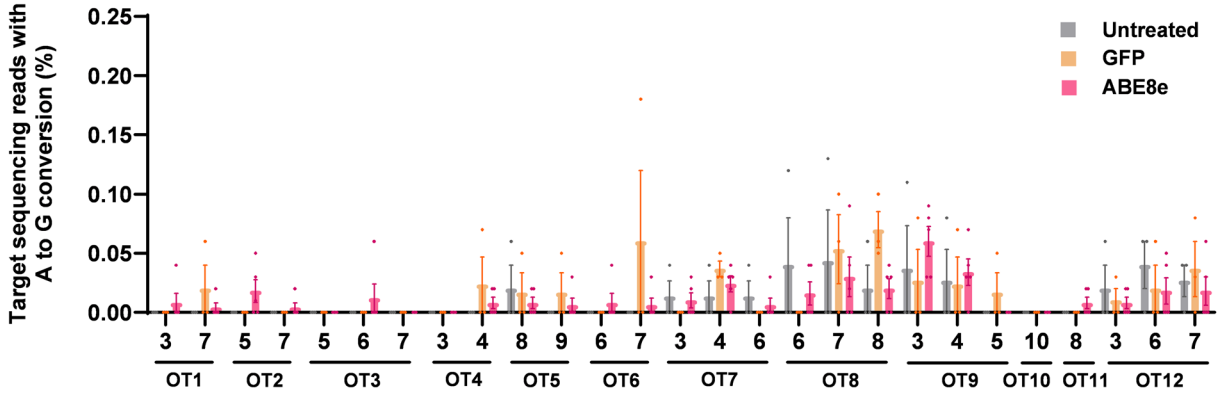

C

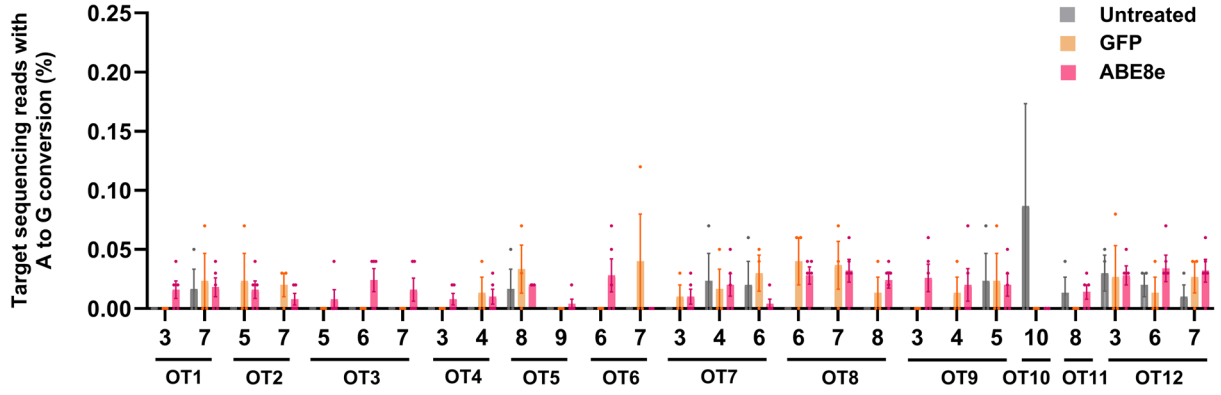

Fig. 3 Confirmation of sgRNA-dependent off-target editing outcomes of gDNA among untreated, GFP and ABE8e-treated mouse brain. **A** Potential sgRNA-dependent twelve off-target sites investigated by Cas-OFFinder software and indicated crRNA sequences and chromosome location information. **B** The base editing efficiencies of twelve off-target sites on frontal cortex in untreated, GFP and ABE8e groups ($n = 3$, each group). **C** The base editing efficiencies of twelve off-target sites on corpus callosum in untreated, GFP and ABE8e groups ($n = 3$, each group). All values are shown as Mean ± SEM

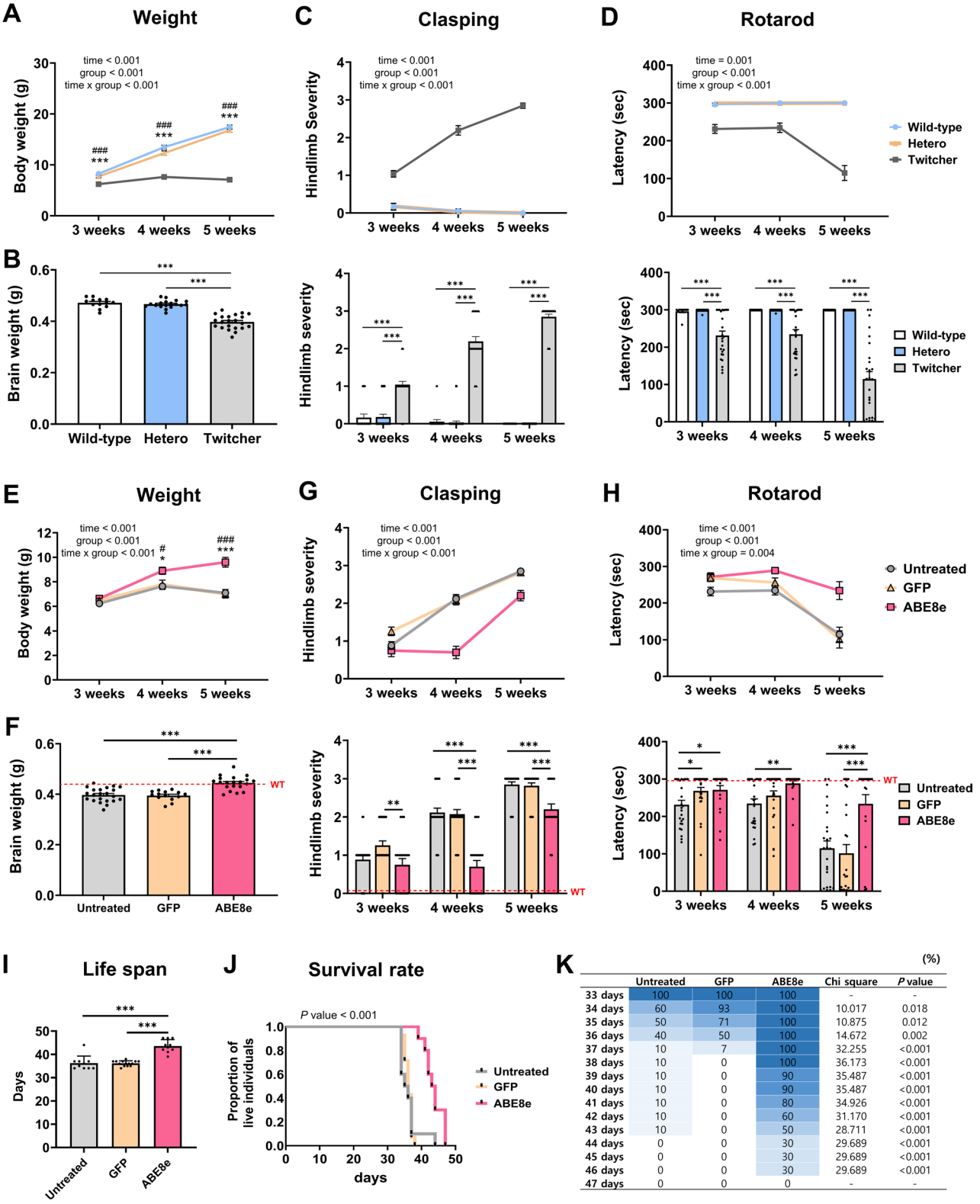

	Untreated	GFP	ABE8e	Chi square	*P* value
33 days	100	100	100	-	-
34 days	60	93	100	10.017	0.018
35 days	50	71	100	10.875	0.012
36 days	40	50	100	14.672	0.002
37 days	10	7	100	32.255	<0.001
38 days	10	0	100	36.173	<0.001
39 days	10	0	90	35.487	<0.001
40 days	10	0	90	35.487	<0.001
41 days	10	0	80	34.926	<0.001
42 days	10	0	60	31.170	<0.001
43 days	10	0	50	28.711	<0.001
44 days	0	0	30	29.689	<0.001
45 days	0	0	30	29.689	<0.001
46 days	0	0	30	29.689	<0.001
47 days	0	0	0	-	-

Fig. 4 (See legend on next page.)

(See figure on previous page.)

Fig. 4 ABE8e alleviate pathological features of the twitcher mouse such as behavioral deterioration and short life span. **A** Body weight measurement showing significant interactions between time and group (WT, $n = 24$; Hetero, $n = 32$, Twitcher, $n = 26$). **B** Brain weight measurement indicating significant decreases in twitcher mice (WT, $n = 13$; Hetero, $n = 18$, Twitcher, $n = 22$). **C** Clasping test, measurement of significant interaction between time and group (WT, $n = 18$; Hetero, $n = 28$, Twitcher, $n = 26$). Twitcher mice showed significant increases in hindlimb severity scores when compared to wild type and heterogeneous groups. **D** Rotarod test at 4 rpm, measurement of the significant interaction between time and group (WT, $n = 12$; Hetero, $n = 17$, Twitcher, $n = 26$). Twitcher mice showed significantly lower latency to fall than wild type and heterogeneous groups. **E** Body weight measurement showing significant interactions between time and group (WT, $n = 26$; GFP, $n = 27$; ABE8e, $n = 20$). **F** Brain weight was significantly increased in ABE-treated groups when compared to untreated and GFP-only groups. (Untreated, $n = 22$; GFP, $n = 14$; ABE8e, $n = 20$). **G** Clasping test, measurement of significant interactions between time and group (Untreated, $n = 26$; GFP, $n = 27$; ABE8e, $n = 20$). The dashed line indicates the WT group. Hindlimb clasping severity scores were significantly decreased in both ABE-treated groups relative to control and GFP-only groups. **H** Rotarod test at 4 rpm, measurement of significant interactions between time and group (Untreated, $n = 26$; GFP, $n = 27$; ABE8e, $n = 20$). The dashed line indicates the WT group. Latency to fall was increased significantly in ABE-treated groups, with the most significant improvements observed at 5 weeks, relative to untreated and GFP-only groups. **I** Lifespan, estimated mean survival period. All statistical results were analyzed by one-way ANOVA (Bonferroni). **J** The result of cumulative survival rates as modeled by the Kaplan-Meier curve, showing the Log-rank test *p*-value. The result of interval survival rate of Kaplan-Meier curve, showing the Log-rank test *p*-value of postnatal days 34 to 47. **K** Table depicts survival rate proportion in all groups using chi-square values, colored in gradient blue according to survival rate percentage (Untreated, $n = 10$; GFP, $n = 14$; ABE8e, $n = 10$). All values are shown as Mean ± SEM with $^{*}P < 0.05$, $^{**}P < 0.01$, $^{***}P < 0.001$. A-F, All analyses used two-way ANOVA test was used to examine main and interaction effects between time and group, followed by Bonferroni *post hoc* test

the distribution of body weight ($P = 0.897$), brain weight ($P = 0.815$), clasping test ($P = 0.656$) and rotarod test ($P = 0.806$; Additional file 2: Table S3) among female and male mice.

To examine the therapeutic outcomes of ABE8e treatment in twitcher mice, all mice were subjected to measurement of body and brain weight, as well as rotarod and clasping tests every week starting from 3 until 5 weeks after birth, as previous studies reported that the phenotypes of twitcher mice rapidly declined after 21 days of age, exhibiting typical neurological symptoms including paralysis in the hind legs and weight loss [29, 30]. The body weights of ABE8e-treated mice (6.63 ± 0.20 g at week 3; 8.90 ± 0.29 g at week 4; 9.60 ± 0.40 g at week 5) were significantly higher than those of untreated and GFP-treated groups ($P < 0.01$ at week 4 and $P < 0.001$ at week 5; 6.22 ± 0.11 g at week 3; 7.64 ± 0.15 g at week 4; 7.09 ± 0.13 g at week 5 and 6.46 ± 0.19 g at week 3; 7.76 ± 0.38 g at week 4; 7.02 ± 0.35 g at week 5, respectively) at 3 ~ 5 weeks demonstrating significant time effect ($F = 21.103$, $P < 0.001$), group effect ($F = 21.103$, $P < 0.001$), and interaction effect (two-way ANOVA, $F = 10.195$, $P < 0.001$; Fig. 4E and Fig. Additional file 1: S4D). Brain weight in ABE8e-treated group (0.445 ± 0.006 g) significantly increased compared to control groups (0.397 ± 0.006 g in untreated group and 0.395 ± 0.005 g in GFP-treated group; $P < 0.001$; Fig. 4F).

We next conducted clasping tests to evaluate the alleviation of progressive symptoms in ABE-treated mice compared to control mice, with significant interactions between time and group at 3 ~ 5 weeks of age (two-way ANOVA, $F = 8.614$, $P < 0.001$). Clasping scores in ABE8e-treated group (0.75 ± 0.16 at week 3; 0.70 ± 0.16 at week 4; 2.20 ± 0.14 at week 5) were apparently lower than those of untreated and GFP-treated groups (0.89 ± 0.10 at week 3; 2.12 ± 0.12 at week 4; 2.85 ± 0.07 at week 5 and 1.26 ± 0.11 at week 3; 2.07 ± 0.19 at week 4; 2.82 ± 0.08 at week 5, respectively) at 4 and 5 weeks of age ($P < 0.001$; Fig. 4G and Additional file 1: Fig. S4E).

Constant speed (4 rpm) rotarod tests in all groups to determine locomotor functions revealed that the motor functions of mice were significantly conserved between time and group (two-way ANOVA, $F = 4.037$, $P = 0.004$), and rotarod performance at 5 weeks were higher in ABE8e-treated group (233.90 ± 24.44 s), compared to untreated and GFP-treated groups (114.73 ± 19.68 s at week 5 and 101.19 ± 23.58 s at week 5, respectively, $P < 0.05$ at week 3; $P < 0.01$ at week 4; $P < 0.001$ at week 5; Fig. 4H and Additional file 1: Fig. S4F).

Additionally, we observed an improvement in lifespan in the ABE8e-treated group (43.60 ± 0.87 days), which exhibited significantly increased mean lifespan up approximately 20 ~ 30%, compared to those in untreated and GFP-treated groups (36.20 ± 0.96 and 36.14 ± 0.29 days, respectively; $P < 0.001$, Fig. 4I). The cumulative survival rate modeled by Kaplan–Meier curve showed a significant difference ($P < 0.001$) in the log-rank test, and the interval survival rate of the Kaplan–Meier curve showed a significant difference in postnatal days 34–46 (Fig. 4J, K). These results suggest treatment with ABE8e delays disease progression by slowing motor deterioration, extending life span, and increasing weight gain in twitcher mice.

To confirm the safety of our treatment methods, ABE8e was administered into WT mice and their progress was closely followed. In WT mice, body weight was measured and all behavioral tests were conducted weekly until 5 weeks of age. Statistical analysis was conducted using both one-way ANOVA and two-way ANOVA. Resultantly, no significant differences in body weight were found in any group (Additional file 1: Fig. S5A). The results of the clasping and rotarod tests revealed no significant differences between control and ABE-treated groups (Additional file 1: Fig. S5B, C). Consequently, these results confirm that ABE treatment with

dual-AAV9 has no apparent effect on the behavioral performance of WT mice.

ABE treatment increases GALC expression, decreases psychosine levels, and improves myelination

A predominant manifestation observed in KD progression is the degradation of the corpus callosum and frontal cortex with a rapid collapse of white matter [28, 48]. Thus, following ICV injection of AAV9-ABE8e on P1, we reasoned that base editing of the target mutation would not only increase GALC activity and reduce psychosine accumulation, but also lead to a consequent improvement in myelination. Given that we confirmed correction of the *Galc* mutation in ABE8e-treated mice, we further corroborated these results with measurement of GALC enzyme activities and psychosine expression levels, the restoration of which is critical for successful therapy. Using samples from both the corpus callosum, which exhibited high ABE expression levels, and white matter rich in myelinated axons, enzyme activity was assayed via calculation of HMU-beta Gal volume in twitcher mice, as previously described [49, 50]. To confirm *Galc* gene expression, the mRNA levels of *Galc* were measured using qRT-PCR. *Galc* mRNA expression was significantly increased in ABE8e-treated groups (1.79 ± 0.06) compared to the GFP-treated and untreated groups (1.00 ± 0.06 and 0.99 ± 0.06, respectively, $P < 0.001$; Fig. 5A). In twitcher mice, it has been reported that PTC-containing mutant *Galc* mRNA is degraded via NMD, resulting in reduced *Galc* mRNA expression compared to that of WT [17]. These results indicated that degradation of non-edited transcripts through NMD may lead to an over-representation of edited cDNA [51]. Consistently, our data demonstrated that ABE8e treatment restored *Galc* mRNA expression in twitcher mice.

In addition, GALC enzyme expression in the corpus callosum was higher in ABE8e-treated groups (65.26 ± 4.58 pmol/mg protein/hr) compared to untreated and GFP-treated groups (39.41 ± 1.05 and 45.09 ± 3.75 pmol/mg protein/hr, respectively, $P < 0.01$; Fig. 5B). Moreover, psychosine levels were quantified in the brain of mice-treated with ABE8e and compared to those of control mice. Mean psychosine levels were reduced by 54–61% in the brain of ABE8e-treated mice (256.45 ± 1.01 pmol/mg) compared to GFP-treated and untreated groups (418.67 ± 6.19 and 470.79 ± 13.68 pmol/mg, respectively, $P < 0.01$; Fig. 5C). These results showed that ABE8e-treatments successfully edit the target base adenine, resulting in increased GALC expression at both RNA and protein levels, and reducing the accumulation of psychosine.

We also measured an increase of MBP at white matter regions via immunohistochemical assays in the proportion of immunoreactive MBP-positive areas. In the corpus callosum, MBP levels in the ABE8e-treated group (22.78 ± 2.84%) were higher than those of untreated and GFP-treated groups (9.93 ± 0.87 and 11.61 ± 0.85%, respectively, $P < 0.001$; Fig. 5D). To confirm the integrity of myelin sheaths and evaluate macrophage infiltration, LFB-PAS staining was performed on the corpus callosum. Further histopathological assessments using LFB-PAS staining demonstrated that LFB staining of myelin was more intense and the corpus callosum was thicker in the ABE8e-treated group compared to both control groups (Fig. 5E, left). Additionally, the number of PAS^+ globoid cells (pink) was significantly reduced in the ABE8e-treated mice (2.83 ± 0.68 PAS^+ cells) compared to untreated and GFP-treated groups (8.08 ± 1.15 PAS^+ cells, $P < 0.05$ and 8.42 ± 1.28 PAS^+ cells, $P < 0.001$, respectively; Fig. 5E, right), indicating decreased microglial activation and demyelination-associated pathology. Taken together, in vivo ABE8e treatment ameliorated KD pathology by restoring GALC activity and enhancing myelin integrity.

Moreover, to confirm there was no presence of pathological dysplasia or tumors in the brain due to use of viral vectors, we stained the cortex, corpus callosum, striatum, hippocampus, thalamus, and cerebellum in all mice using hematoxylin and eosin staining. Analysis of these various brain regions indicated no histological changes resulting from AAV-mediated tumor formation (Fig. S6).

Imaging-based analyses confirmed amelioration of myelin deficits following ABE treatment

Therapeutic outcomes of KD treatment have also been confirmed using electron microscopy and MRI methods [52–55]. The advantages of using these methods include effective visualization of both the appearance and count of axons by displaying image results alongside numerical data.

First, we conducted MRI for mice of all groups on postnatal day 38. Several types of DTI were used to evaluate the structural integrity of the white matter fiber tract (Fig. 6A). Confirming the increase of axial diffusion through in vivo ABE treatments, the FA and AD of ABE8e-treated group (0.234 ± 0.008 in FA; 0.961 ± 0.019%, in AD) was remarkably higher than untreated and GFP-treated groups (0.188 ± 0.005 and 0.198 ± 0.003, respectively, in FA; 0.836 ± 0.024 and 0.867 ± 0.012, respectively, in AD) in the corpus callosum ($P < 0.001$ in FA; $P < 0.01$ for GFP, $P < 0.001$ for untreated in AD, Fig. 6B, C). Additionally, radial diffusion after in vivo ABE8e treatment was also decreased, with the RD and MD of ABE8e-treated groups (0.712 ± 0.018 in RD; 0.787 ± 0.016% in MD) remarkably lower than untreated and GFP-treated groups (0.995 ± 0.039 and 0.838 ± 0.017%, respectively, in RD; 0.942 ± 0.028 and 0.911 ± 0.012%, respectively, in MD) in the corpus callosum ($P < 0.01$ for GFP, $P < 0.001$ for untreated in RD; $P < 0.001$ in MD, Fig. 6D, E).

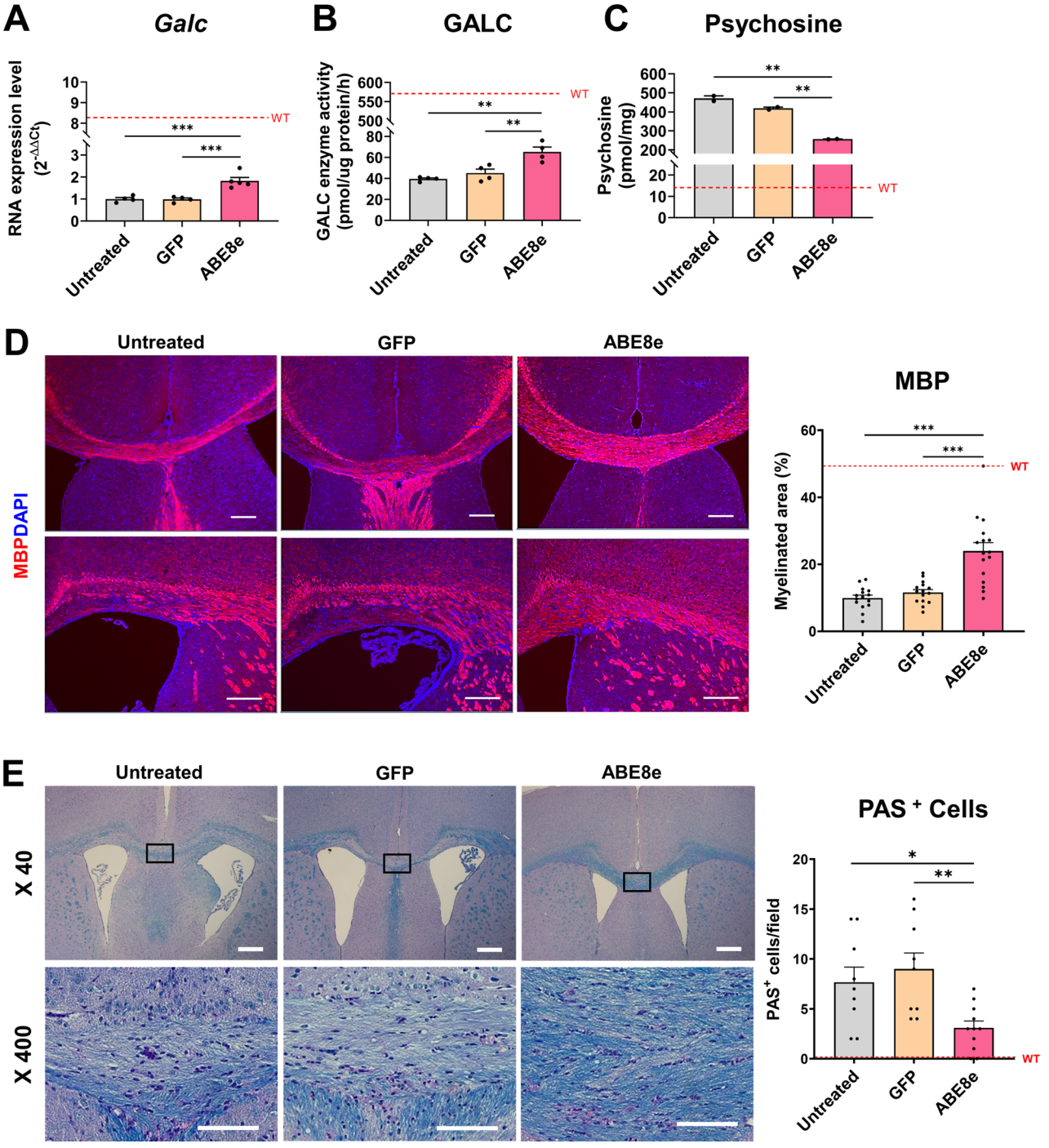

Fig. 5 Base editing by split-ABE8e restores GALC expression and myelination in the brain of twitcher mice. **A** mRNA expression of Galc using qRT-PCR. *Galc* expression was significantly induced by split-ABE8e in the corpus callosum of twitcher mice ($n=4$, each group) **B** GALC enzyme activity (protein volume of HMU-βGal) was significantly increased following treatment of split-ABE8e in the corpus callosum of twitcher mice ($n=4$, each group). **C** Psychosine was significantly reduced following treatment of split-ABE8e in the brain of twitcher mice ($n=2$, each group). **D** The representative images for DAPI (blue) and MBP (red) in the central corpus callosum and the lateral corpus callosum. Total MBP-positive area, including the central corpus callosum and the lateral corpus callosum in the ABE8e-treated group, was increased compared to that of untreated and GFP-treated groups. In particular, the MBP-positive area was higher in the ABE8e-treated group than in the control groups. ($n=16$ from 4 samples, each group). Scale bars: 100 µm. **E** Representative images of LFB-PAS staining in the corpus callosum of Twitcher mice. LFB-stained myelin (blue) appeared thicker and better preserved in the corpus callosum of the ABE8e-treated group compared to the control groups. The number of PAS^+ globoid cells (pink) was reduced in the ABE8e-treated group (Untreated, $n=3$; GFP, $n=3$; ABE8e, $n=4$). Scale bars: 100 µm. A-C, Mean ± SEM. $^*P<0.05$, $^{**}P<0.01$, $^{***}P<0.001$. The dashed line indicates the WT group in all graphs. All statistical results were analyzed by one-way ANOVA (Bonferroni)

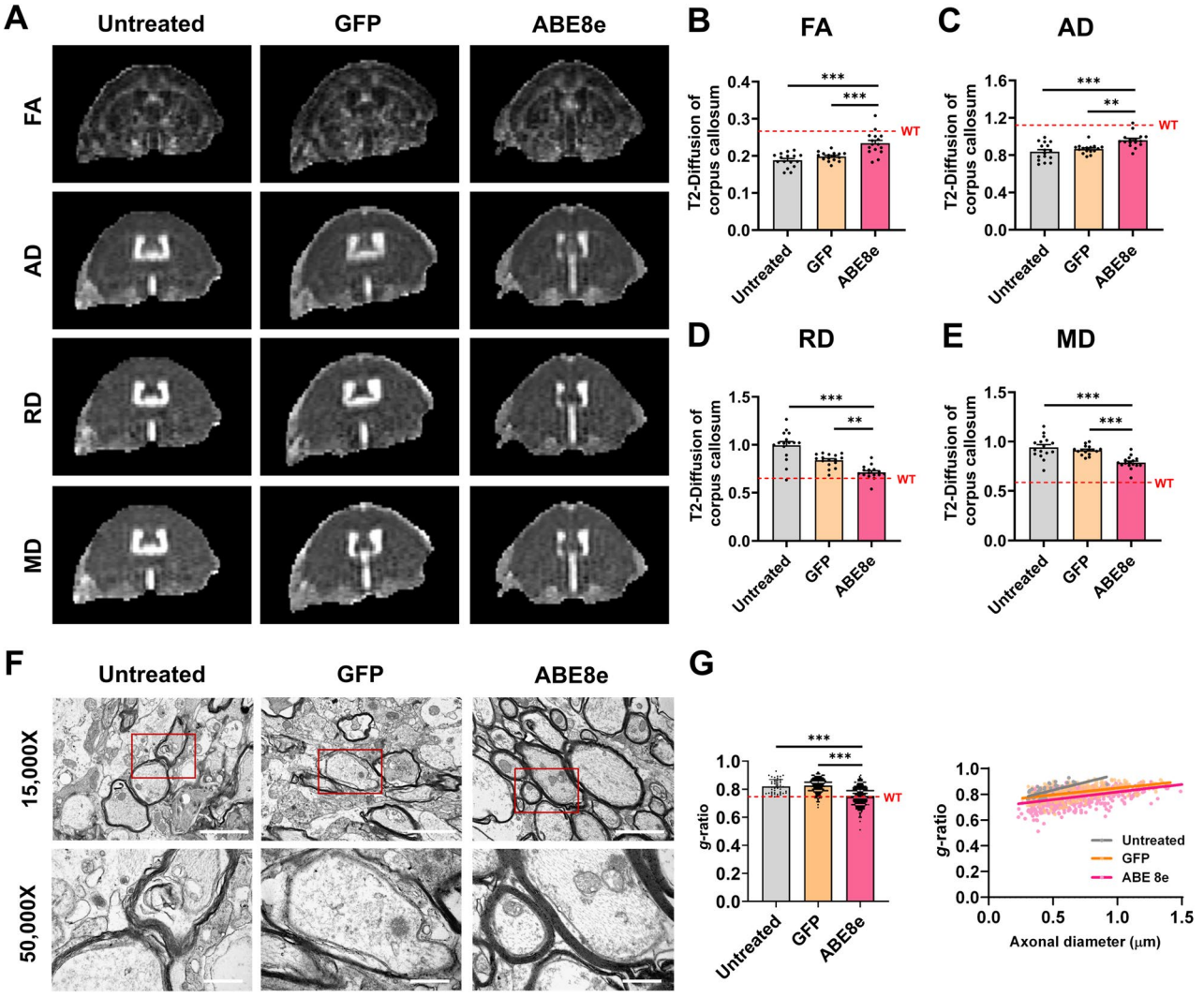

Fig. 6 Base editing by split-ABE8e induced axonal recovery and integrity in the corpus callosum. **A** Representative images showing axons in the corpus callosum. **B**-**E** Representative figures were analyzed according to four DTI parameters. **B** and **C** The FA quantification axial diffusion expression in the corpus callosum ($n = 16$ from 4 samples, each group). The AD quantification axial diffusion expression in the corpus callosum ($n = 16$ from 4 samples, each group). The FA and AD of ABE8e-treated group was remarkably brighter than untreated and GFP-treated groups in the corpus callosum. **D** and **E** The RD quantification axial diffusion expression in the corpus callosum, ($n = 16$ from 4 samples, each group). The MD quantification axial diffusion expression in the corpus callosum ($n = 16$ from 4 samples, each group). The RD and MD of ABE8e-treated group was remarkably darker than untreated and GFP-treated groups. **F** Representative TEM photomicrographs of the corpus callosum in twitcher mice show improved myelination and remyelination following ABE8e treatment. **G** Notably, the g-ratio in the ABE8e-treated group was significantly lower than that of the untreated group (Untreated, $n = 2$; GFP, $n = 3$; ABE8e, $n = 2$). Scale bars: 2000 nm at 15,000X and 500 nm at 50,000X. The dashed line indicates the WT group in all graphs. All statistical results were analyzed by one-way ANOVA (Bonferroni) and shown as Mean ± SEM with $^{*}P < 0.05$, $^{**}P < 0.01$, $^{***}P < 0.001$

We also qualified the state of myelin sheath layers through TEM in the corpus callosum. Representative photomicrographs of the corpus callosum showed conserved axonal integrity, with axons sheathed in dense and compact myelin in the brains of ABE8e-treated mice (Fig. 6F). Quantitative analysis of g-ratios in the corpus callosum showed a significant reduction in the ABE8e-treated group (0.7792 ± 0.0024) compared to the untreated group and GFP group (0.8205 ± 0.0073, $P < 0.001$ and 0.8172 ± 0.0031, $P < 0.001$, respectively; Fig. 6G, left), indicating thicker myelin relative to axonal diameter. Linear regression of g-ratio versus axonal diameter further confirmed this trend, as the ABE8e-treated group exhibited a downward shift in the regression line compared to control groups, suggesting enhanced remyelination across a range of axon calibers (Fig. 6G, right). Taken together, in vivo ABE8e treatment improved myelination by enhancing axonal integrity and promoting remyelination.

ABE8e-treated mice display broad phenotypic and molecular recovery relative to WT controls

Most of outcomes is expressed as the percentage of recovery, with values of untreated mutant mice defined as 0 and those in WT mice defined as 100. The ABE8e-treated group showed measurable functional and pathological improvements. At 5 weeks post-treatment, the clasping score improved by ~ 23% and the rotarod performance reached ~ 64% of the WT phenotype. Body and brain weights were restored to ~ 24% and ~ 64% of WT values, respectively (Additional file 2: Table S4).

At the molecular level, *Galc* mRNA increased ~ 9%, GALC enzymatic activity recovered ~ 5% and psychosine accumulation was reduced by ~ 47% relative to WT. Additionally, MBP density increased by approximately 34%, and PAS-positive cells decreased by approximately 65%. Consistent with these findings, diffusion-weighted MRI and g-ratio restored by 35–78% and 59% relative to WT (Additional file 2: Table S5). Collectively, these data indicate that ABE8e-mediated correction, though limited in efficiency, is sufficient to elicit substantial metabolic and structural recovery in the central nervous system (CNS).

Discussion

Recent advances in in vitro base editing have provided valuable proof-of-concept evidence for correcting pathogenic point mutations in monogenic diseases. ABEs effectively corrected a mutation of the retinal pigment epithelium-specific 65 kDa protein (*RPE65*) gene in a retinal degeneration 12 cell line, restoring RPE65 protein expression with an editing efficiency of approximately 25–40% [56]. Similarly, PAX6 nonsense mutations were edited by ABEs up to 76.8%correction efficiency in humanized mouse embryonic stem cells [57]. In addition, using CBEs and ABEs to convert toxic CAG repeats to CAA in Huntington's disease patient fibroblasts, achieving ~ 15–20% editing and reduced mutant HTT toxicity [58]. Especially, Leal et al. reviewed BE-mediated approaches for lysosomal storage disorders, including GALC, and reported restoration of GALC enzyme activity and reduction of psychosine in patient-derived fibroblasts and hematopoietic progenitor cells after precise nucleotide correction [59].

Base editing technologies have shown therapeutic potential in the treatment of genetic disorders affecting the retina, liver, and CNS [38, 60–62]. Recent studies have demonstrated the therapeutic potential of in vivo adenine and cytosine base editors delivered by AAV to introduce a stop codon in prion-like protein gene (*PRNP*) of humanized prion mice in prion diseases by targeting the *PRNP* gene [63]. Similarly, precise single-base correction without double-strand breaks achieved phenotypic rescue in prion mouse models [64]. Taken together, these BE studies establish a foundation for translating precise single-nucleotide correction strategies into in vivo therapeutic approaches for neurogenetic and neurodegenerative diseases. Based on these results, the principal advance of the present study lies in demonstrating that in vivo genomic correction of mutant *Galc*, the cause of KD, using ABE8e may represent a viable therapeutic strategy. Further, dual-AAV9 treatment with ABE8e did not adversely affect the behavioral functions of WT mice, nor cause any dysplasia or tumor formation the KD brain. Ultimately, through the in vivo administration of BEs in the twitcher mouse KD model, behavioral assessments confirmed that ABE treatment significantly ameliorates disease progression and alleviates functional motor deterioration.

In vivo gene editing studies indicate that even limited correction can produce significant phenotypic recovery in mouse models of monogenic disorders and amyotrophic lateral sclerosis (ALS). In Duchenne muscular dystrophy models, ~ 2% genomic correction and restoration of only ~ 8% dystrophin protein were sufficient to improve muscle strength [65]. Similarly, genome editing with < 1% indel frequency markedly delayed disease onset and extended survival in an ALS model [66]. Moreover, Daly et al. defined ~ 1% of normal β-glucuronidase activity as a therapeutic threshold capable of reversing pathological substrate accumulation in lysosomal storage disorders [67]. Collectively, these findings indicate that low genome editing efficacy or low-level enzymatic restoration can have meaningful functional outcomes. Therefore, our findings of a 0.5% gDNA correction rate and an 8% restoration of GALC enzyme activity support at least a partial phenotypic recovery, even if they do not result in a marked extension of survival in a mouse model of KD.

In order to deliver split ABE genes to the diseased mouse model, we selected the CNS-targeting AAV9 vector due to its wide application at both preclinical and clinical stages of treatment for various diseases [68]. According to previous reports, AAV9 exhibits the highest transduction efficiency at 3 ~ 4 weeks, which is sustained for 3 ~ 6 months [39–41]. We assumed that these characteristics made it highly suitable for therapeutic use in twitcher mice, given that phenotypic disease manifestations rapidly progress after 3 weeks (postnatal day 21) until natural death. The lack of detectable harmful or off-target effects in our results suggests that AAV9-ABE treatments were able to alleviate disease progression through restoration of GALC expression and activity.

Previous in vivo studies using dual-AAV base editor systems have reported similar in vivo efficiencies with dosages in various murine organs with injected concentrations of 1×10^9 vg each of N- and C-terminal AAVs yielding approximately 1% base editing efficiency in the

liver [69], 3×10^9 vg yielding 3.6% efficiency in the eye [62], and 5×10^{10} vg yielding 2.8% efficiency in the cortex of the brain [70]. Recent studies utilizing higher AAV doses (6×10^{11}~2×10^{12} vg/μL) have predominantly adopted systemic routes of administration [38, 71]. In contrast, the direct intraparenchymal or ICV administration of AAV at concentrations exceeding 10^{13} GC/mL has been shown to induce local inflammation, disruption of the blood–brain barrier (BBB), and neuronal toxicity [72]. Consistent with these observations, high-titer AAV9 (≥ 10^{13} GC/mL) was reported to cause marked astrocyte and microglial activation accompanied by neuronal loss in the mouse brain [73], and Guo et al. similarly observed BBB disruption and immune cell infiltration at comparable concentrations [74]. Therefore, we used 1×10^{10} GC (per hemisphere) dose of AAV9 for practical and safety considerations. Nevertheless, future studies employing higher AAV dose or lentivirus, as well as non-viral vectors, will be essential to further validate our findings and improve in vivo editing efficiency.

Although ABE8e exhibited higher editing efficacy in human cells, ABE8e also catalyzes cytosine deamination at a preferred motif (TC*N) and generates transcriptome-wide sgRNA-independent off-target RNA editing [14, 75]. To bypass this issue, a more precise version of ABE, named ABE8eWQ which reduced both cytosine deamination activity and off-target RNA editing [18]. Nevertheless, given its highest editing efficacy among tested ABE variants in MEFs derived from twitcher mice, we selected ABE8e for in vivo therapeutic application.

GALC protein expression has been reported in up to 73% of neurons, 11% of oligodendrocyte-lineage cells, 18% of astrocytes, and 7% of microglia in the brains of perinatal mice with KD [76]. These finding suggest that restoration of GALC in a single cell type may be insufficient for the treatment of KD, and that GALC expression across multiple neural cell types is essential. In addition, several studies have demonstrated that ICV injection is the most efficient route to administer treatments throughout the entire brain [77, 78]. Timing of ICV injection is also reported to be important for treatment efficacy. Because our study was conducted via ICV injection at P1, we specifically assessed the site-specific correction efficiency across brain regions. Therefore, rather than analyzing cells individually, we focused on identifying regions with high correction rates through brain region-by-region analysis and verifying their effectiveness. AAV9-ABE administration via ICV injection is associated with relatively few systemic side effects. However, at the same time, it is difficult to effectively target to both the CNS and the peripheral nervous system (PNS), which presumably disallows targeting of mutant *GALC* expressed in Schwann cells surrounding peripheral nerves, and thus restoration of peripheral myelination. These properties of the delivery system used in our study may explain why ABE treatment could not sufficiently prevent symptom development and early death in twitcher mice.

Editing efficiencies reaching approximately 50–60% in liver and CNS have been reported to be associated with phenotypic rescue in monogenic disorders by in vivo base editing [38, 79, 80]. However, we attribute the relatively low correction efficiency observed in our work primarily to the need to use SpCas9-NG at a suboptimal PAM site. While SpCas9-NG enables targeting beyond canonical NGG sites, its on-target editing activity is often lower than that of the WT SpCas9 at NGG PAMs [81]. Considering these results, treatment effects should be optimized using different injection methods. Recent studies in gene delivery have reported various approaches aimed at developing improved injection methods and identifying optimal regions for injection [78, 82–84]. Due to the lack of overall viral distribution, we believe that future administration of viral vectors would be further improved with systemic administration rather than local ICV injection [78, 85]. To determine the most efficient way to deliver ABE genes, we suggest several further studies: first, experimental evaluation of the efficacy of ABE administration via different injection routes can be considered. Various AAV injection routes have already been established, such as intraperitoneal [86], intravenous [87], and intramuscular [88] injection, which may enable the injected material to better reach peripheral nerves. Second, rather than simply repairing the *GALC* gene, some groups have seen success with modifying the enzyme itself to improve secretion efficiency [89]. Third, recent efforts have focused on strategies to improve in vivo correction efficiency by non-viral delivery systems such as lipid nanoparticles (LNPs) and engineered virus-like particles (eVLPs). In recent research, LNP formulations were demonstrated to be capable of crossing the BBB or achieving widespread neural transfection through *in utero* delivery, enabling efficient gene correction in neuronal tissues [90, 91]. Meanwhile, VLP-based transient ribonucleoprotein delivery allows precise and integration-free gene editing in retinal and neuronal tissues [92, 93]. These non-viral strategies are emerging as promising approaches that can increase correction efficiency while minimizing potential adverse effects, such as immune response, apoptosis, and genome integration. Utilizing three-pronged approaches to optimize the extensive delivery of gene-editing machinery, while also modifying the target gene itself to improve in vivo efficiency and safety, may represent an effective strategy to ensure sufficient production of functional GALC enzyme, thereby promoting the restoration of myelination in both the CNS and PNS.

Conclusions

Dual-AAV9 treatment with ABE8e rescued the PTC in the mutant *Galc* gene as well as expression of *Galc* mRNA levels and GALC enzyme activity while reducing psychosine accumulation, consequently increasing myelination and ameliorating behavioral deterioration in a model of KD. Therapeutic application of ABE-mediated gene correction technology thus may provide potential for expanding the therapeutic arsenal against genetic diseases caused by guanine-to-adenine point mutations.

Abbreviations

KD	Krabbe disease
GALC	galactosylceramidase
AAV	Adeno-associated virus
DSBs	DNA double strand breaks
BEs	base editors
CBEs	cytosine base editors
ABEs	adenine base editors
nCas9	Cas9 nickase
PTC	premature termination codon
TadA	tRNA-specific adenosine deaminase
NMD	nonsense-mediated mRNA decay
TEM	transmission electron microscopy
MRI	magnetic resonance imaging
WT	wild-type
MEFs	mouse embryonic fibroblasts
P1	postnatal day 1
ICV	intracerebroventricular
gDNA	genomic DNA
cDNA	complementary DNA
qRT-PCR	quantitative reverse transcription PCR
IHC	immunohistochemistry
MBP	myelin basic protein
DTI	diffusion tensor imaging
FA	fractional anisotropy
AD	axial diffusivity
RD	radial diffusivity
MD	mean diffusivity
LFB/PAS	luxol fast blue/ periodic acid schiff
TEM	transmission electron microscopy
H&E	hematoxylin and eosin
PAM	protospacer-adjacent motif
NGS	next-generation sequencing
PE	prime editing
NC	negative control
RPE65	RPE65
CNS	central nervous system
PRNP	prion-like protein gene
ALS	amyotrophic lateral sclerosis
PNS	peripheral nervous system
BBB	blood-brain barrier
LNPs	lipid nanoparticles
VLPs	engineered virus-like particles

Supplementary Information

The online version contains supplementary material available at https://doi.org/10.1186/s13073-026-01620-2.

Additional file 1: Figure S1. Database of GALC mutations in patients with Krabbe disease. Figure S2. Confirmation of various base editing patterns and GALC enzyme structure prediction. Figure S3. In vivo transcriptome-wide sgRNA-independent off-target RNA editing in selective brain and tissue regions. Figure S4. ABE8e alleviate pathological features of the twitcher mice such as behavioral deterioration. Figure S5. AAV9-split-ABE8e treatment does not significantly alter behavioral outcomes in wild-type mice. Figure S6. AAV9-split-ABE8e treatment does not induce tumorigenesis or dysplasia in wild-type mice. Table S1. The sequence of sgRNA and primers for qRT-PCR. Table S2. The sequence of primers for NGS. Table S3. The relationship between male and female distributions in behavior tests, body and brain weight analyses of twitcher mice. Table S4. Functional and phenotypic outcomes expressed as the percentage of recovery relative to wild-type at 5 weeks of age. Table S5. Therapeutic and pathological outcomes expressed as the percentage of recovery relative to wild-type at 5 weeks of age.

Acknowledgements

MID (Medical Illustration & Design), as a member of the Medical Research Support Services of Yonsei University College of Medicine, providing excellent support with medical illustration. Most analysis of sequence data was carried out using the computing sever at the Genomic Medicine Institute Research Service Center.

Authors' contributions

S.B. and S.-R.C. conceived this project; B.-G.N. performed most of the in vitro and in vivo study; J.H.S. performed the animal study and contributed to analyze data and write the manuscript; S.-A.H. contributed to the in vitro study and analyzed data; J.-H.K. managed the animals and performed the animal study; M.K. contributed to data analysis; G.R.N contributed to write and finalize the manuscript; Y.H. and S.C. contributed to the animal study; All authors read and approved the final manuscript.

Funding

This research was supported by the Korean Health Technology R&D Project through the Korea Health Industry Development Institute (KHIDI), funded by the Ministry of Health & Welfare, Republic of Korea (no. HI22C1588 to S.-R.C and S.C., HI21C1314, RS-2022-KH129545 and RS-2025-02215487 to S.-R.C.), the National Research Foundation of Korea (NRF) (no. 2021M3A9H3015389 to S.B.), the Korean Fund for Regenerative Medicine (KFRM) grant funded by the Korea government (no. RS-2024-00332601 to S.B.), and Basic Science Research Program through the NRF funded by the Ministry of Education (no. RS-2024-00404132 to B.-G.N and RS-2025-25437527 to J.H.S.).

Data availability

Targeted deep sequencing data have been deposited in the Sequence Read Archive (SRA) under accession number PRJNA1346310. Plasmids used in this study will be made available through Addgene upon publication. All other data supporting the findings of this study are included within the article and its additional files.

Declarations

Ethics approval and consent to participate

This study did not involve human participants. All animal was housed in a facility accredited by the Association for Assessment and Accreditation of Laboratory Animal Care (AAALAC) and all the experiments were approved by the Institutional Animal Care and Use Committee (IACUC) of Yonsei University Health System (permit number: 2020-0029, 2020-0047).

Consent for publication

Not applicable.

Competing interests

The authors declare no competing interests.

Author details

[1]Department and Research Institute of Rehabilitation Medicine, Yonsei University College of Medicine, Seoul 03722, Republic of Korea
[2]Medical Research Center of Genomic Medicine Institute, Seoul National University College of Medicine, Seoul 03080, Republic of Korea
[3]Graduate Program of Biomedical Engineering, Yonsei University College of Medicine, Seoul 03722, Republic of Korea
[4]Department of Biohealth Engineering, Graduate school of Transdisciplinary Health Sciences, Yonsei University, Seoul 03722, Republic of Korea
[5]Graduate School of Medical Science, Brain Korea 21 Project, Yonsei University College of Medicine, Seoul 03722, Republic of Korea

[6]AAVATAR Therapeutics, 12925 Gyeonggi-do, Republic of Korea
[7]Department of Biomedical Sciences, Seoul National University College of Medicine, Seoul 03080, Republic of Korea
[8]Cancer Research Institute, Seoul National University College of Medicine, Seoul 03080, Republic of Korea
[9]Rehabilitation Institute of Neuromuscular Disease, Yonsei University College of Medicine, Seoul 03722, Republic of Korea
[10]Brain Research Institute, Yonsei University College of Medicine, Seoul 03722, Republic of Korea
[11]Metabolism-Dementia Research Institute, Yonsei University College of Medicine, Seoul 03722, Republic of Korea

Received: 9 July 2025 / Accepted: 3 March 2026
Published online: 23 April 2026

References

1. Wenger DA, Escolar ML, Luzi P, Rafi MA. Krabbe disease (Globoid Cell Leukodystrophy). In: Valle DL, Antonarakis S, Ballabio A, Beaudet AL, Mitchell GA, editors. The Online Metabolic and Molecular Bases of Inherited Disease. New York, NY: McGraw-Hill Education; 2019.
2. Hagberg B, Sourander P, Svennerholm L. Diagnosis of Krabbe's infantile leucodystrophy. J Neurol Neurosurg Psychiatry. 1963;26:195–8.
3. Duffner PK, Barczykowski A, Jalal K, Yan L, Kay DM, Carter RL. Early infantile Krabbe disease: results of the World-Wide Krabbe Registry. Pediatr Neurol. 2011;45:141–8.
4. Suzuki K, Suzuki Y. Globoid cell leucodystrophy (Krabbe's disease): deficiency of galactocerebroside beta-galactosidase. Proc Natl Acad Sci U S A. 1970;66:302–9.
5. Miyatake T, Suzuki K. Globoid cell leukodystrophy: additional deficiency of psychosine galactosidase. Biochem Biophys Res Commun. 1972;48:539–43.
6. Page KM, Stenger EO, Connelly JA, Shyr D, West T, Wood S, et al. Hematopoietic Stem Cell Transplantation to Treat Leukodystrophies: Clinical Practice Guidelines from the Hunter's Hope Leukodystrophy Care Network. Biol Blood Marrow Transpl. 2019;25:e363–74.
7. Yoon IC, Bascou NA, Poe MD, Szabolcs P, Escolar ML. Long-term neurodevelopmental outcomes of hematopoietic stem cell transplantation for late-infantile Krabbe disease. Blood. 2021;137:1719–30.
8. Liu M, Zhang W, Xin C, Yin J, Shang Y, Ai C, et al. Global detection of DNA repair outcomes induced by CRISPR-Cas9. Nucleic Acids Res. 2021;49:8732–42.
9. Kosicki M, Tomberg K, Bradley A. Repair of double-strand breaks induced by CRISPR-Cas9 leads to large deletions and complex rearrangements. Nat Biotechnol. 2018;36:765–71.
10. Papathanasiou S, Markoulaki S, Blaine LJ, Leibowitz ML, Zhang CZ, Jaenisch R, et al. Whole chromosome loss and genomic instability in mouse embryos after CRISPR-Cas9 genome editing. Nat Commun. 2021;12:5855.
11. Zuccaro MV, Xu J, Mitchell C, Marin D, Zimmerman R, Rana B, et al. Allele-Specific Chromosome Removal after Cas9 Cleavage in Human Embryos. Cell. 2020;183:1650–64. e15.
12. Gaudelli NM, Komor AC, Rees HA, Packer MS, Badran AH, Bryson DI, et al. Programmable base editing of A*T to G*C in genomic DNA without DNA cleavage. Nature. 2017;551:464–71.
13. Komor AC, Kim YB, Packer MS, Zuris JA, Liu DR. Programmable editing of a target base in genomic DNA without double-stranded DNA cleavage. Nature. 2016;533:420–4.
14. Richter MF, Zhao KT, Eton E, Lapinaite A, Newby GA, Thuronyi BW, et al. Phage-assisted evolution of an adenine base editor with improved Cas domain compatibility and activity. Nat Biotechnol. 2020;38:883–91.
15. Gopalappa R, Lee M, Kim G, Jung ES, Lee H, Hwang HY, et al. In vivo adenine base editing rescues adrenoleukodystrophy in a humanized mouse model. Mol Ther. 2024;32:2190–206.
16. Peters CW, Hanlon KS, Ivanchenko MV, Zinn E, Linarte EF, Li Y, et al. Rescue of hearing by adenine base editing in a humanized mouse model of Usher syndrome type 1F. Mol Ther. 2023;31:2439–53.
17. Lee WC, Tsoi YK, Dickey CA, Delucia MW, Dickson DW, Eckman CB. Suppression of galactosylceramidase (GALC) expression in the twitcher mouse model of globoid cell leukodystrophy (GLD) is caused by nonsense-mediated mRNA decay (NMD). Neurobiol Dis. 2006;23:273–80.
18. Jeong YK, Lee S, Hwang GH, Hong SA, Park SE, Kim JS, et al. Adenine base editor engineering reduces editing of bystander cytosines. Nat Biotechnol. 2021;39:1426–33.
19. Sakai N, Inui K, Tatsumi N, Fukushima H, Nishigaki T, Taniike M, et al. Molecular cloning and expression of cDNA for murine galactocerebrosidase and mutation analysis of the twitcher mouse, a model of Krabbe's disease. J Neurochem. 1996;66:1118–24.
20. Landrum MJ, Lee JM, Riley GR, Jang W, Rubinstein WS, Church DM, et al. ClinVar: public archive of relationships among sequence variation and human phenotype. Nucleic Acids Res. 2014;42:D980–5.
21. Landrum MJ, Lee JM, Benson M, Brown G, Chao C, Chitipiralla S, et al. ClinVar: public archive of interpretations of clinically relevant variants. Nucleic Acids Res. 2016;44:D862–8.
22. Hwang GH, Park J, Lim K, Kim S, Yu J, Yu E, et al. Web-based design and analysis tools for CRISPR base editing. BMC Bioinformatics. 2018;19:542.
23. Bae S, Park J, Kim JS. Cas-OFFinder: a fast and versatile algorithm that searches for potential off-target sites of Cas9 RNA-guided endonucleases. Bioinformatics. 2014;30:1473–5.
24. Clement K, Rees H, Canver MC, Gehrke JM, Farouni R, Hsu JY, et al. CRISPResso2 provides accurate and rapid genome editing sequence analysis. Nat Biotechnol. 2019;37:224–6.
25. Abramson J, Adler J, Dunger J, Evans R, Green T, Pritzel A, et al. Accurate structure prediction of biomolecular interactions with AlphaFold 3. Nature. 2024;630:493–500.
26. Burley SK, Bhatt R, Bhikadiya C, Bi C, Biester A, Biswas P, et al. Updated resources for exploring experimentally-determined PDB structures and Computed Structure Models at the RCSB Protein Data Bank. Nucleic Acids Res. 2025;53:D564–74.
27. Feltri ML, Weinstock NI, Favret J, Dhimal N, Wrabetz L, Shin D. Mechanisms of demyelination and neurodegeneration in globoid cell leukodystrophy. Glia. 2021;69:2309–31.
28. Inamura N, Kito M, Go S, Kishi S, Hosokawa M, Asai K, et al. Developmental defects and aberrant accumulation of endogenous psychosine in oligodendrocytes in a murine model of Krabbe disease. Neurobiol Dis. 2018;120:51–62.
29. Cantuti-Castelvetri L, Maravilla E, Marshall M, Tamayo T, D'Auria L, Monge J, et al. Mechanism of neuromuscular dysfunction in Krabbe disease. J Neurosci. 2015;35:1606–16.
30. Graziano AC, Cardile V. History, genetic, and recent advances on Krabbe disease. Gene. 2015;555:2–13.
31. Ezer S, Zuckerman S, Segel R, Zlotogora J. Carrier screening for Krabbe disease in an isolated inbred community. Am J Med Genet A. 2022;188:2555–9.
32. Orsini JJ, Kay DM, Saavedra-Matiz CA, Wenger DA, Duffner PK, Erbe RW, et al. Newborn screening for Krabbe disease in New York State: the first eight years' experience. Genet Med. 2016;18:239–48.
33. Kaiser T, Allen HM, Kwon O, Barak B, Wang J, He Z et al. MyelTracer: A Semi-Automated Software for Myelin g-Ratio Quantification. eNeuro. 2021;8(4):ENEURO.0558-20.2021. https://doi.org/10.1523/ENEURO.0558-20.2021.
34. Endo M, Mikami M, Endo A, Kaya H, Itoh T, Nishimasu H, et al. Genome editing in plants by engineered CRISPR-Cas9 recognizing NG PAM. Nat Plants. 2019;5:14–7.
35. QiuL Q, Lai WS, Stumpo DJ, Blackshear PJ. Mouse Embryonic Fibroblast Cell Culture and Stimulation. Bio Protoc. 2016;6(13):e1859. https://doi.org/10.21769/BioProtoc.1859.
36. Tan YS, Lei YL. Generation and Culture of Mouse Embryonic Fibroblasts. Methods Mol Biol. 2019;1960:85–91.
37. Ryu SM, Koo T, Kim K, Lim K, Baek G, Kim ST, et al. Adenine base editing in mouse embryos and an adult mouse model of Duchenne muscular dystrophy. Nat Biotechnol. 2018;36:536–9.
38. Levy JM, Yeh WH, Pendse N, Davis JR, Hennessey E, Butcher R, et al. Cytosine and adenine base editing of the brain, liver, retina, heart and skeletal muscle of mice via adeno-associated viruses. Nat Biomed Eng. 2020;4:97–110.
39. Kim JY, Grunke SD, Levites Y, Golde TE, Jankowsky JL. Intracerebroventricular viral injection of the neonatal mouse brain for persistent and widespread neuronal transduction. J Vis Exp. 2014. https://doi.org/10.3791/51863.51863.
40. Chakrabarty P, Rosario A, Cruz P, Siemienski Z, Ceballos-Diaz C, Crosby K, et al. Capsid serotype and timing of injection determines AAV transduction in the neonatal mice brain. PLoS ONE. 2013;8:e67680.
41. Kim JY, Ash RT, Ceballos-Diaz C, Levites Y, Golde TE, Smirnakis SM, et al. Viral transduction of the neonatal brain delivers controllable genetic mosaicism

for visualising and manipulating neuronal circuits in vivo. Eur J Neurosci. 2013;37:1203–20.
42. Li PP, Margolis RL. Use of single guided Cas9 nickase to facilitate precise and efficient genome editing in human iPSCs. Sci Rep. 2021;11:9865.
43. Lee J, Lim K, Kim A, Mok YG, Chung E, Cho SI, et al. Prime editing with genuine Cas9 nickases minimizes unwanted indels. Nat Commun. 2023;14:1786.
44. Hanlon KS, Kleinstiver BP, Garcia SP, Zaborowski MP, Volak A, Spirig SE et al. High levels of AAV vector integration into CRISPR-induced DNA breaks. Nat Commun. 2019;10(1):4439. https://doi.org/10.1038/s41467-019-12449-2.
45. Kabadi AM, Mejia-Guerra MK, Graef JD, Khan SZ, Walton EM, Wang XZ et al. AAV-based CRISPR-Cas9 genome editing: Challenges and engineering opportunities. Curr Opin Biomedical Eng. 2024;29:100517. https://doi.org/10.1016/j.cobme.2023.100517.
46. Grunewald J, Zhou R, Garcia SP, Iyer S, Lareau CA, Aryee MJ, et al. Transcriptome-wide off-target RNA editing induced by CRISPR-guided DNA base editors. Nature. 2019;569:433–7.
47. Beltran-Quintero ML, Bascou NA, Poe MD, Wenger DA, Saavedra-Matiz CA, Nichols MJ, et al. Early progression of Krabbe disease in patients with symptom onset between 0 and 5 months. Orphanet J Rare Dis. 2019;14:46.
48. Niu J, Yu G, Wang X, Xia W, Wang Y, Hoi KK, et al. Oligodendroglial ring finger protein Rnf43 is an essential injury-specific regulator of oligodendrocyte maturation. Neuron. 2021;109:3104–18. e6.
49. Szymanska K, Lugowska A, Laure-Kamionowska M, Bekiesinska-Figatowska M, Gieruszczak-Bialek D, Musielak M, et al. Diagnostic difficulties in Krabbe disease: a report of two cases and review of literature. Folia Neuropathol. 2012;50:346–56.
50. Del Grosso A, Galliani M, Angella L, Santi M, Tonazzini I, Parlanti G, et al. Brain-targeted enzyme-loaded nanoparticles: A breach through the blood-brain barrier for enzyme replacement therapy in Krabbe disease. Sci Adv. 2019;5:eaax7462.
51. Popp MW, Maquat LE. Leveraging Rules of Nonsense-Mediated mRNA Decay for Genome Engineering and Personalized Medicine. Cell. 2016;165:1319–22.
52. Kim JH, Yu JE, Chang BJ, Nahm SS. Neonatal influenza virus infection affects myelination in influenza-recovered mouse brain. J Vet Sci. 2018;19:750–8.
53. Cappello V, Marchetti L, Parlanti P, Landi S, Tonazzini I, Cecchini M, et al. Ultrastructural Characterization of the Lower Motor System in a Mouse Model of Krabbe Disease. Sci Rep. 2016;6:1.
54. Kelm ND, West KL, Carson RP, Gochberg DF, Ess KC, Does MD. Evaluation of diffusion kurtosis imaging in ex vivo hypomyelinated mouse brains. NeuroImage. 2016;124:612–26.
55. Manno FAM, Isla AG, Manno SHC, Ahmed I, Cheng SH, Barrios FA, et al. Early Stage Alterations in White Matter and Decreased Functional Interhemispheric Hippocampal Connectivity in the 3xTg Mouse Model of Alzheimer's Disease. Front Aging Neurosci. 2019;11:39.
56. Wu Y, Wan X, Zhao D, Chen X, Wang Y, Tang X, et al. AAV-mediated base-editing therapy ameliorates the disease phenotypes in a mouse model of retinitis pigmentosa. Nat Commun. 2023;14:4923.
57. Adair BA, Korecki AJ, Djaksigulova D, Wagner PK, Chiu NY, Lam SL, et al. ABE8e Corrects Pax6-Aniridic Variant in Humanized Mouse ESCs and via LNPs in Ex Vivo Cortical Neurons. Ophthalmol Ther. 2023;12:2049–68.
58. Choi DE, Shin JW, Zeng S, Hong EP, Jang JH, Loupe JM et al. Base editing strategies to convert CAG to CAA diminish the disease-causing mutation in Huntington's disease. Elife. 2024;12:RP89782. https://doi.org/10.7554/eLife.89782.1.
59. Leal AF, Prieto LE, Pachajoa H. CRISPR/Cas-Based Ex Vivo Gene Therapy and Lysosomal Storage Disorders: A Perspective Beyond Cas9. Cells. 2025;14(15):1147. https://doi.org/10.3390/cells14151147.
60. Koblan LW, Erdos MR, Wilson C, Cabral WA, Levy JM, Xiong ZM, et al. In vivo base editing rescues Hutchinson-Gilford progeria syndrome in mice. Nature. 2021;589:608–14.
61. Su J, She K, Song L, Jin X, Li R, Zhao Q, et al. In vivo base editing rescues photoreceptors in a mouse model of retinitis pigmentosa. Mol Ther Nucleic Acids. 2023;31:596–609.
62. She K, Liu Y, Zhao Q, Jin X, Yang Y, Su J, et al. Dual-AAV split prime editor corrects the mutation and phenotype in mice with inherited retinal degeneration. Signal Transduct Target Ther. 2023;8:57.
63. An M, Davis JR, Levy JM, Serack FE, Harvey JW, Brauer PP, et al. In vivo base editing extends lifespan of a humanized mouse model of prion disease. Nat Med. 2025;31:1319–28.
64. Schindeler A, Chu J, Au-Yeung C, Kao HY, Ginn SL, O'Donohue AK. In vivo precision base editing to rescue mouse models of disease. Mol Ther Nucleic Acids. 2025;36:102622.
65. Nelson CE, Hakim CH, Ousterout DG, Thakore PI, Moreb EA, Castellanos Rivera RM, et al. In vivo genome editing improves muscle function in a mouse model of Duchenne muscular dystrophy. Science. 2016;351:403–7.
66. Gaj T, Ojala DS, Ekman FK, Byrne LC, Limsirichai P, Schaffer DV. In vivo genome editing improves motor function and extends survival in a mouse model of ALS. Sci Adv. 2017;3:eaar3952.
67. Daly TM, Vogler C, Levy B, Haskins ME, Sands MS. Neonatal gene transfer leads to widespread correction of pathology in a murine model of lysosomal storage disease. Proc Natl Acad Sci U S A. 1999;96:2296–300.
68. DiMattia MA, Nam HJ, Van Vliet K, Mitchell M, Bennett A, Gurda BL, et al. Structural Insight into the Unique Properties of Adeno-Associated Virus Serotype 9. J Virol. 2012;86:6947–58.
69. Davis JR, Wang X, Witte IP, Huang TP, Levy JM, Raguram A, et al. Efficient in vivo base editing via single adeno-associated viruses with size-optimized genomes encoding compact adenine base editors. Nat Biomed Eng. 2022;6:1272–83.
70. Davis JR, Banskota S, Levy JM, Newby GA, Wang X, Anzalone AV, et al. Efficient prime editing in mouse brain, liver and heart with dual AAVs. Nat Biotechnol. 2024;42:253–64.
71. Su J, Jin X, She K, Liu Y, Song L, Zhao Q, et al. In vivo adenine base editing corrects newborn murine model of Hurler syndrome. Mol Biomed. 2023;4:6.
72. Ye D, Chukwu C, Yang Y, Hu Z, Chen H. Adeno-associated virus vector delivery to the brain: Technology advancements and clinical applications. Adv Drug Deliv Rev. 2024;211:115363.
73. Stone D, Aubert M, Jerome KR. Breaching the blood-brain barrier: AAV triggers dose-dependent toxicity in the brain. Mol Ther Methods Clin Dev. 2023;31:101105.
74. Guo Y, Chen J, Ji W, Xu L, Xie Y, He S, et al. High-titer AAV disrupts cerebrovascular integrity and induces lymphocyte infiltration in adult mouse brain. Mol Ther Methods Clin Dev. 2023;31:101102.
75. Kim HS, Jeong YK, Hur JK, Kim JS, Bae S. Adenine base editors catalyze cytosine conversions in human cells. Nat Biotechnol. 2019;37:1145–8.
76. Favret J, Nawaz MH, Patel M, Khaledi H, Gelb M, Shin D. Perinatal loss of galactosylceramidase in both oligodendrocytes and microglia is crucial for the pathogenesis of Krabbe disease in mice. Mol Ther. 2024;32:2207–22.
77. Slavc I, Cohen-Pfeffer JL, Gururangan S, Krauser J, Lim DA, Maldaun M, et al. Best practices for the use of intracerebroventricular drug delivery devices. Mol Genet Metab. 2018;124:184–8.
78. Belur LR, Romero M, Lee J, Podetz-Pedersen KM, Nan Z, Riedl MS, et al. Comparative Effectiveness of Intracerebroventricular, Intrathecal, and Intranasal Routes of AAV9 Vector Administration for Genetic Therapy of Neurologic Disease in Murine Mucopolysaccharidosis Type I. Front Mol Neurosci. 2021;14:618360.
79. Lim CKW, Gapinske M, Brooks AK, Woods WS, Powell JE, Zeballos CM, et al. Treatment of a Mouse Model of ALS by In Vivo Base Editing. Mol Ther. 2020;28:1177–89.
80. Zuo Y, Zhang C, Zhou Y, Li H, Xiao W, Herzog RW, et al. Liver-specific in vivo base editing of Angptl3 via AAV delivery efficiently lowers blood lipid levels in mice. Cell Biosci. 2023;13:109.
81. Nishimasu H, Shi X, Ishiguro S, Gao L, Hirano S, Okazaki S, et al. Engineered CRISPR-Cas9 nuclease with expanded targeting space. Science. 2018;361:1259–62.
82. Daci R, Flotte TR. Delivery of Adeno-Associated Virus Vectors to the Central Nervous System for Correction of Single Gene Disorders. Int J Mol Sci. 2024;25(2):1050. https://doi.org/10.3390/ijms25021050.
83. Zhou K, Han J, Wang Y, Zhang Y, Zhu C. Routes of administration for adeno-associated viruses carrying gene therapies for brain diseases. Front Mol Neurosci. 2022;15:988914.
84. Huang Q, Chan KY, Wu J, Botticello-Romero NR, Zheng Q, Lou S, et al. An AAV capsid reprogrammed to bind human transferrin receptor mediates brain-wide gene delivery. Science. 2024;384:1220–7.
85. Pan X, Sands SA, Yue Y, Zhang K, LeVine SM, Duan D. An Engineered Galactosylceramidase Construct Improves AAV Gene Therapy for Krabbe Disease in Twitcher Mice. Hum Gene Ther. 2019;30:1039–51.
86. Machida A, Kuwahara H, Mayra A, Kubodera T, Hirai T, Sunaga F, et al. Intraperitoneal administration of AAV9-shRNA inhibits target gene expression in the dorsal root ganglia of neonatal mice. Mol Pain. 2013;9:36.
87. Kagiava A, Richter J, Tryfonos C, Leal-Julia M, Sargiannidou I, Christodoulou C, et al. Efficacy of AAV serotypes to target Schwann cells after intrathecal and intravenous delivery. Sci Rep. 2021;11:23358.
88. Tosolini AP, Sleigh JN. Intramuscular Delivery of Gene Therapy for Targeting the Nervous System. Front Mol Neurosci. 2020;13:129.

89. Ricca A, Cascino F, Morena F, Martino S, Gritti A. In vitro Validation of Chimeric beta-Galactosylceramidase Enzymes With Improved Enzymatic Activity and Increased Secretion. Front Mol Biosci. 2020;7:167.
90. Gao K, Han H, Cranick MG, Zhao S, Xu S, Yin B, et al. Widespread Gene Editing in the Brain via In Utero Delivery of mRNA Using Acid-Degradable Lipid Nanoparticles. ACS Nano. 2024;18:30293–306.
91. Cao D, Hou X, Wang C, Wang S, Liu Z, Tian M, et al. Lipid nanoparticles for mRNA delivery in brain via systemic administration. Sci Adv. 2025;11:eadw0730.
92. An M, Raguram A, Du SW, Banskota S, Davis JR, Newby GA, et al. Engineered virus-like particles for transient delivery of prime editor ribonucleoprotein complexes in vivo. Nat Biotechnol. 2024;42:1526–37.
93. Ling S, Zhang X, Dai Y, Jiang Z, Zhou X, Lu S, et al. Customizable virus-like particles deliver CRISPR-Cas9 ribonucleoprotein for effective ocular neovascular and Huntington's disease gene therapy. Nat Nanotechnol. 2025;20:543–53.

Publisher's note